Final Report

Project Title:	Research and Development for Novel Thermal Energy Storage Systems (TES) for Concentrating Solar Power (CSP)
Project Period:	2/27/2009 – 6/30/2013
Project Budget:	$1,290,362
Submission Date:	9/1/2008
Recipient:	University of Connecticut
Address:	191 Auditorium Road Storrs, CT 06269-3139, USA
Award Number:	DE-FG36-08GO18146
Project Teams:	University of Connecticut, University of Kansas, Virginia Tech
Contacts:	P.I.: Amir Faghri Department of Mechanical Engineering University of Connecticut 191 Auditorium Road Storrs, CT 06269-3139, USA Co P.I.: Theodore L. Bergman Department of Mechanical Engineering The University of Kansas 1530 West 15th Street Lawrence, KS 66045, USA Co P.I.: Ranga Pitchumani Department of Mechanical Engineering Virginia Tech 103 Randolph Hall Blacksburg, VA 24060, USA

Executive Summary:

The overall objective was to develop innovative heat transfer devices and methodologies for novel thermal energy storage systems for concentrating solar power generation involving phase change materials (PCMs). Specific objectives included embedding thermosyphons and/or heat pipes (TS/HPs) within appropriate phase change materials to significantly reduce thermal resistances within the thermal energy storage system of a large-scale concentrating solar power plant and, in turn, improve performance of the plant. Experimental, system level and detailed comprehensive modeling approaches were taken to investigate the effect of adding TS/HPs on the performance of latent heat thermal energy storage (LHTES) systems. Experimental results proved the superior performance of HPs to increase the heat transfer rates compared to finned and non-finned cases. Quantitatively, inclusion of heat pipes increased PCM melting rates by approximately 60%, while the fins were not as effective. During solidification, the heat pipe-assisted configuration transferred approximately twice the energy between a heat transfer fluid and the PCM, relative to both the fin-assisted LHTES and the non-heat pipe, non-fin configurations.

Comprehensive multiphase multi-dimensional simulations were conducted to provide a better understanding of the fundamental physical phenomena involved in thermal energy storage in a phase change media with embedded TS/HPs, and also to provide input for the system level model. A system level model, leveraged by the input from the comprehensive model, was developed to predict the response of large-scale TS/HP-assisted LHTES systems in a computationally-effective manner. Consistent with the experimental results, the results of the system level model also demonstrated a significant increase in heat transfer rates associated with HP-assisted LHTES systems.

The developed system level model was employed to predict the performance of a large-scale LHTES system utilizing multiple PCMs in a cascaded configuration. It was shown that the maximum exergy recovery can be achieved by using a cascaded configuration. Optimization studies were performed using the system level model and the preferred configurations of HPs in the LHTES systems were identified. Exergy analysis of LHTES systems was carried out considering the practical constraints imposed on the system in solar applications. Novel guidelines were proposed for design and optimization of LHTES systems for solar applications. Economic aspects of TS/HP-assisted LHTES systems were also investigated and it was shown that these systems are cost competitive with the state of the art thermal energy storage systems currently in use.

Table of Contents

Background:..... 4
Introduction:..... 7
Project Results and Discussion: 7
Conclusions: 40
Path Forward: 40
References: 41
List of peer-reviewed journal articles produced during the course of the project: . 49

Background:

Energy storage capability is desirable in solar and wind electric power applications due to the intermittent nature of the energy generated. In solar thermal generation, thermal energy storage is the preferred energy storage mode [1–10]. Three major categories are be identified in thermal energy storage: (i) sensible heat storage, typically in a solid or liquid media; (ii) latent heat thermal energy storage which utilizes the heat of fusion of a phase change material as it melts and solidifies; and (iii) thermochemical storage, in which thermal energy is stored or released as the chemical bonds are formed or broken [11]. Latent heat thermal energy storage (LHTES) exhibits desirable attributes relative to sensible thermal energy storage due to the high energy storage density corresponding to LHTES. However, the low thermal conductivity of phase change materials (PCMs) has limited the use of LHTES in emerging applications such as large scale power generation in conjunction with concentrating solar technologies. Novel LHTES systems have recently been receiving increased research attention to improve the heat transfer rates, thereby reducing the size and cost of the storage system (e.g., [12–16]).

In general, in a LHTES system applicable to solar thermal electricity production a heat transfer fluid (HTF) exchanges energy with a PCM. The HTF may be delivered from solar collectors, in which case the PCM is melted. Alternatively, the HTF may represent the working fluid of a Rankine or other power cycle or may be an intermediate fluid to transfer energy to a power cycle, in which case the PCM is the energy source and undergoes solidification. In either case, large temperature differences between the HTF and the PCM are undesirable. Several approaches have been suggested to reduce the thermal resistance between the HTF and the PCM including: packing the PCM within a high thermal conductivity solid matrix [17–20], introducing high thermal conductivity particles into the PCM [21,22], increasing the area for heat transfer that separates the HTF from the PCM by utilizing extended surfaces or fins [23–29], or encapsulating the PCM within the HTF [30–33].

Other investigations have focused on the incorporation of several PCMs, each with a unique phase change temperature, and have shown that cascading several PCMs can result in higher heat transfer rates, as well as improved exergy (or second law) efficiencies [13,15,34–37]. The improvements offered by cascaded PCMs are due to a more uniform temperature difference between the hot and cold media compared to a non-cascaded LHTES system. Representative investigations of LHTES with cascaded PCMs follow. Watanabe et al. [37] numerically investigated a low temperature, packed bed LHTES with PCMs having a spatially-linear (along the HTF flow direction) melting temperature distributions. The LHTES system consisted of PCM-packed, horizontal cylindrical tubes in a rectangular shell with water as the shell side HTF. The investigators considered the effect of the distribution of the PCMs on the exergy efficiency as well as charging (melting) and discharging (solidification) rates. They found that setting the melting temperatures to an optimal distribution reduces the melting and solidification times. The investigators also demonstrated the higher exergy efficiency of a LHTES system with PCMs having multiple phase change temperatures.

A theoretical analysis of a cascaded LHTES system consisting of an infinite number of individual PCMs with different melting temperatures along the HTF flow

stream was conducted by Aceves et al. [34]. For a charging process, as well as an overall charging-discharging process, the optimal PCM phase change temperature distribution was found to be an exponential function of the axial location along the HTF flow direction. It was shown that for charging- and overall charging-discharging processes the exergy efficiency of the cascaded LHTES is higher than that of single PCM systems. In a related study, Gong and Mujumdar [36] numerically investigated a shell-and-tube LHTES setup in which the HTF tube is surrounded by segments of PCMs with different melting temperatures. Alternating melting and freezing processes were simulated. The results demonstrated that use of multiple PCMs enhanced heat transfer relative to a single PCM. Gong and Mujumdar [35] also analytically investigated cascaded LHTES systems with two, three and five PCMs, and concluded that the exergy efficiency can be increased by a factor of two to three with use of more than one PCM. They also studied the order in which the PCMs make contact with the HTF, and found that the PCMs should be arranged in a particular manner to obtain optimal performance.

Cui et al. [13] analyzed the thermal performance of a 2 kW solar receiver thermal storage module with three PCMs contained in annular canisters adjoining HTF tubes. The PCM melting temperatures ranged from 717°C to 779°C, and a gaseous mixture of He and Xe was specified as the HTF. The results indicated that the cascaded LHTES provides increased heat transfer rates and more steady HTF outlet temperatures over time, compared with a single PCM. In other solar-related work, Michels and Pitz–Paal [15] investigated, experimentally and numerically, a cascaded LHTES with alkali nitrate salt PCMs for use in parabolic trough power plants. The experiments were conducted using a vertical shell-and-tube heat exchanger with three PCM segments under a HTF temperature range of 280°C to 350°C. In addition, a numerical analysis was carried out on a cascaded LHTES with five PCMs. Their results confirmed the enhanced performance of a cascaded LHTES compared to non-cascaded systems with respect to the total amount of the PCMs that melt and solidify. They also concluded that alternative PCMs with a high heat of fusion and with low corrosivity would be desirable, and that the PCM thermal conductivities should be increased to 2 W/m.K for the cascaded LHTES to be successfully applied to parabolic trough plants.

An alternative approach is to incorporate devices such as heat pipes (HPs) to serve as thermal conduits between the HTF and the PCM [38,39]. It is well known that HPs have very high effective thermal conductivities, can be tuned to operate passively in specific temperature ranges through selection of appropriate working fluids and operating pressures, and can be fabricated in a variety of shapes [40]. Moreover, compared to solid fins of similar dimensions heat pipes have a low thermal capacitance, further improving PCM melting or solidification rates. The HP transfers heat from the HTF to the PCM with evaporation and condensation of the HP working fluid occurring at the end sections of the HP which are separated by an adiabatic section.

Review of the literature reveals that a limited number of theoretical and experimental studies have been carried out to investigate the performance of hybrid HP-PCM systems. Liu et al. [41] studied experimentally a HP heat exchanger for latent energy storage. They considered a LHTES similar to that of Horbaniuc et al. [42], but with a circumferentially-finned thermosyphon. Experiments were conducted using water as the HTF and an industrial paraffin wax with T_m = 52.1°C as the PCM. A copper

thermosyphon charged with acetone and an operating temperature range of 0 - 100 °C was utilized. The experiments were designed to investigate the effect of the HTF inlet temperature and flow rate on phase change and heat transfer rates.

Tardy et al. [43] investigated, numerically and experimentally, the thermal behavior of heat pipes involving melting of a low-melting-temperature PCM. They used an apparatus consisting of 32 HPs with their upper halves inserted into a cold storage tank containing ice, and their lower halves placed in a warmer, ducted air stream. A thermal resistance model was developed to determine the heat transfer rates from the air stream to the ice tank and the associated melting process, but water solidification was not studied. In other related work, Etheridge et al. [44] provided field test data regarding the performance of a hybrid PCM-HP cooling system for conditioning of air in buildings. The HPs were half-embedded in a hydrated Glauber's salt which was used as the PCM with the other half of the HPs exposed to air which was used to heat or cool a room. Both charging and discharging were considered. Lee et al. [45] employed a thermosyphon to enhance the heat transfer in a low-melting-temperature PCM. The experimental results were associated with the use of a variety of different PCMs during charging and discharging, with attention paid on the sensitivity of system performance on the various storage materials used.

Theoretical modeling of a hybrid HP-PCM system involves simulation of conjugated heat transfer in both heat pipe and PCM. A number of different models of varying complexity have been proposed to simulate heat pipe behavior [40]. They range from analytical models (e.g. [46,47]) to detailed 3D numerical models (e.g. [48]). A representative model of intermediate complexity is the HPTAM, a transient 2D model developed by Tournier and El-Genk [49,50], which is capable of determining the liquid–vapor interfacial dynamics and liquid pooling of the heat pipe working fluid. However, the HPTAM utilizes an assumption that the working fluid vapor is always saturated, which may not be satisfied in reality. In models developed by Cao and Faghri [51] as well as Rice and Faghri [52], the vapor is assumed to be saturated only at the wick surface while the transport equations are solved in the vapor region.

The process of PCM melting including the effects of natural convection in the liquid phase has been extensively investigated using numerical simulation. Representative studies of PCM melting in rectangular enclosures are Ho and Viskanta [53], Webb and Viskanta [54], Bergman and Webb [55], and Cao and Faghri [56]. Simulation of melting in cylindrical enclosures has also received considerable attention. The early work of Sparrow et al. [57] considered melting that is induced from a vertical isothermal cylindrical surface placed concentrically in a cylindrical enclosure housing a PCM. The model involved use of a coordinate transformation to describe the evolving shape of the melt region, and an implicit finite difference approach was employed to simulate natural convection in the melt. Representative of later work, Ismail and Melo [58] developed a finite volume model with a vorticity and stream function formulation to describe the free convection in the molten phase, while Jones et al. [59] combined a finite volume approach with an apparent heat capacity formulation to account for the absorption of latent energy.

The solidification in a hybrid HP-PCM system was analytically studied by Horbaniuc et al. [42]. They considered a LHTES system that was able to operate in three modes; charging (melting the PCM), discharging (solidifying the PCM) and

simultaneous charging and discharging. Their analysis considered the two-dimensional growth of solid PCM around the evaporator of the HP as well as adjacent to the fins. They demonstrated that inclusion of more fins leads to increased solidification rates, and concluded that the duration of freezing can be controlled by varying the number of fins. Liu et al. [41] presented a thermal resistance analysis to investigate the heat transfer in a LHTES system.

Introduction:

The need persists to continually decrease the capital cost of concentrating solar power, and a major opportunity is the development of novel thermal energy storage schemes. These schemes collect excess solar energy during the day, store it, and release the stored thermal energy to generate electric power at night or during overcast conditions. Advantages of thermal energy storage coupled with concentrating solar power include, but are not limited to: (i) a better match between power generation and diurnal swings in electricity demand and (ii) decreased size and cost of hardware (e.g. turbines and pumps) corresponding to 24-hour thermal energy storage-enabled leveling of power generation. Hence, the levelized cost of energy is reduced, and the overall plant capacity factor is increased with thermal energy storage.

This research focuses on use of phase change materials as the thermal energy storage medium. In contrast to other thermal energy storage media (for example, sensible energy storage), the size of the thermal energy storage system can be reduced, directly reducing the cost of plant construction. Unfortunately, most thermal energy storage media are characterized by very low thermal conductivities, making transfer of thermal energy to or from the various solid-liquid interfaces within the media difficult. The unique aspect of the project is to embed thermosyphons or heat pipes in the phase change material to reduce the thermal resistance between the location where phase change occurs, and the working fluid of the power cycle. (A thermosyphon is typically an enclosed tube that contains a working fluid which evaporates at the bottom of the tube and condenses at the top, with the condensate returned to the bottom evaporator by gravity. Augmentation of heat transfer rates occurs in one direction only due to phase change, so thermosyphons are sometimes referred to as thermal diodes. A heat pipe is similar, but contains a wicking material, with the condensate returned to the evaporator by surface tension forces (capillary action); the evaporator of a heat pipe can be placed above the condensing section. Either device can provide an effective thermal conductivity that is up to 90 (ninety) times that of copper [40]. Either device transfers large amounts of energy nearly isothermally, can be custom-tailored in performance by carefully selecting the working fluid and its operating pressure, as well as the wall material, and can be fabricated in a wide variety of shapes.)

Project Results and Discussion:

Experimental:

Robak et al. [60] experimentally investigated latent heat thermal energy storage utilizing heat pipes or fins. Photographic observations, melting and solidification rates, and PCM energy storage quantities are reported. Heat pipe effectiveness is defined and used to quantify the relative performance of heat pipe-assisted and fin-assisted

configurations to situations involving neither heat pipes nor fins. For the experimental conditions of this study, inclusion of heat pipes increases PCM melting rates by approximately 60%, while the fins are not as effective. During solidification, the heat pipe-assisted configuration transfers approximately twice the energy between a heat transfer fluid and the PCM, relative to both the fin-assisted LHTES and the non-heat pipe, non-fin configurations.

An overall schematic of the experimental apparatus is shown in Fig. 1a. As shown in Fig. 1b, the test cell consists of a vertical, cylindrical PCM enclosure and underlying heat exchanger. The acrylic enclosure has an inside diameter of 127 mm, a height of 200 mm, and a wall thickness of 6 mm. It is mounted to a heat exchanger that serves as the heat source (sink) for melting (solidification). The cylinder is mated to the heat exchanger by way of a 7-mm wide, 4-mm deep channel housing a synthetic rubber O-ring. Two heat exchangers were utilized; the first with a plane top surface for benchmark experiments involving neither HPs nor fins. The second heat exchanger incorporated a top plate that was modified to accommodate heat pipes or fins. A paraffin, n-octadecane ($C_{18}H_{38}$, T_f = 27.5°C) of 99% purity was used as the PCM and distilled water was used as the HTF.

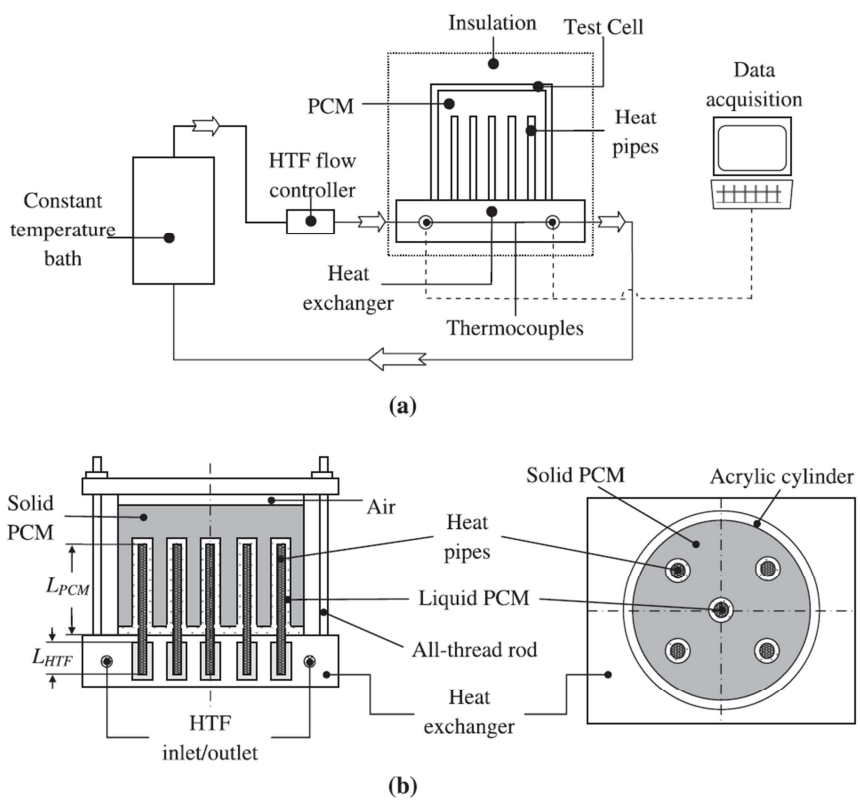

Fig. 1. (a) Schematic of overall experimental setup. (b) Detailed diagram.

Fig. 2a shows the energy stored in the PCM for the benchmark, heat pipe, and fin experiments. Three distinct melting regimes appear in all three cases. The first corresponds to a relatively rapid accumulation of energy in the PCM within the first 10 min of each experiment, when maximum temperature differences exist between the

HTF and the contents of the test cell. The second regime is associated with a nearly steady heat transfer rate to the PCM, as natural convection proceeds with a relatively time-invariant heat transfer coefficient between the solid surfaces and the solid–liquid interface(s). A third regime corresponds to a sudden increase in the heat transfer rate due to close contact melting. As expected, the charging rate is lowest (highest) for the benchmark (heat pipe-assisted) case. The discharged energy is shown in Fig. 2b for the benchmark, HP-assisted, and fin-assisted experiments. Because the process is, in large part, conduction-dominated the heat transfer rates diminish with time. The heat released from the PCM was largest for the HP-assisted case, while the fin-assisted case was found to perform only slightly better than the benchmark.

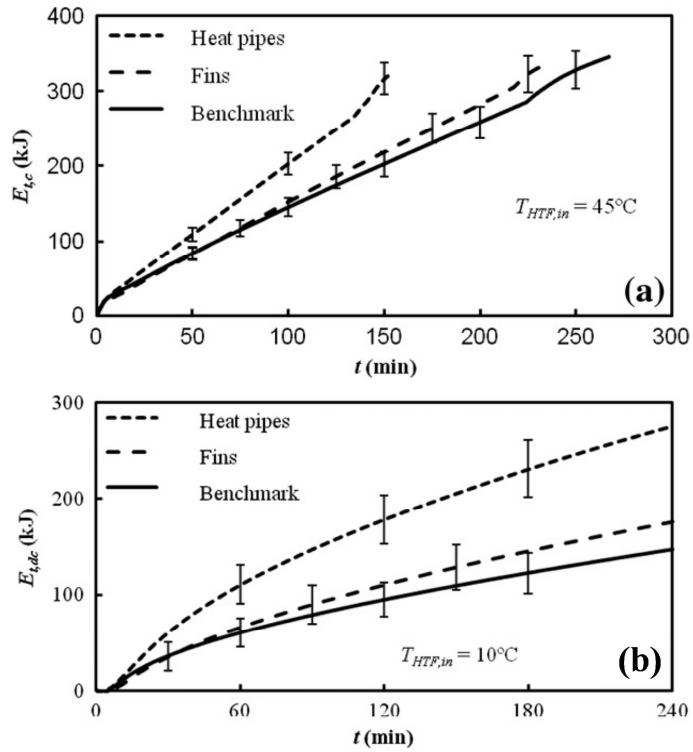

Fig. 2. (a) Energy stored in the PCM for the benchmark, HP-assisted and fin-assisted cases; $T_{HTF,in}$ = 45°C and $\dot{m}_{HTF}$ = 0.0026 kg/s, (b) Energy released from PCM for the benchmark, HP-assisted and fin-assisted cases; $T_{HTF,in}$ = 10°C and $\dot{m}_{HTF}$ = 0.0022 kg/s.

Sharifi et al. [61] conducted experiments in order to generate detailed data associated with the outward melting of a PCM induced by a heated rod that is placed concentrically within a cylindrical enclosure. Heat transfer and melting effects in a base-case configuration consisting of a vertically-oriented enclosure are successfully simulated with an established two-dimensional numerical model, partially validating the experimental apparatus and procedure. Experimental measurements indicate that modest tilting of the test cell significantly affects measured local temperatures within the PCM, as well as the temporal evolution of the solid morphology as it melts. The modification is attributed to the establishment of three-dimensional flow within the molten PCM. The experimental data for the tilted enclosure cases might be used to

validate three-dimensional models for PCM melting in geometrical configurations relevant to, for example, latent heat thermal energy storage systems.

A schematic of the test cell is shown in Fig. 3. The PCM is housed in a vertically-orientated enclosure with an inside diameter and height of 45.8 mm and 18.9 mm, respectively. The enclosure is formed by a cylindrical acrylic tube of wall thickness 4.6 mm, and two 6.4 mm thick top and bottom Teflon plates. The joints between the plates and the cylinder are sealed with compressed synthetic rubber O-rings, and a 10 mm diameter pure copper rod of length 82 mm is secured concentrically in the bottom plate with a brass Swagelok fitting. The bottommost portion of the rod is wrapped in a 38.2 mm long electric resistance heater (Minco 9449) which is powered with a Protek dual DC power supply. The entire test cell is wrapped with a 20 mm thick fiber glass blanket. To provide additional insulation, a second 127 mm ID acrylic cylinder is installed over the test cell, creating a 11.5 mm air gap. The entire apparatus is placed on a metallic plate that can be tilted to angles $0° < \theta < 20°$ from the vertical. The test cell can also be rotated about an azimuthal angle. The uncertainty in the tilt and azimuthal angles is ±1 degree. A paraffin wax, n-octadecane (99% pure $C_{18}H_{38}$) with melting temperature of 28°C and heat of fusion of 243.5 kJ/kg is used as the PCM.

Temperature data are obtained from 8 Teflon-coated, 254 μm diameter chromel-alumel (K-type) thermocouples that are held in place with a yoke constructed of an acrylic tube within the PCM. The thermocouple beads are all located in a single / plane. Prior to installation the thermocouples were calibrated at both the freezing and boiling points of water, and the estimated error in measured temperatures is ±0.1°C. Thermocouple voltages are collected using a National Instruments data acquisition system, and Labview software is used to process the voltages and record temperatures. Photographs of the PCM are taken using a 10-megapixel Nikon digital camera.

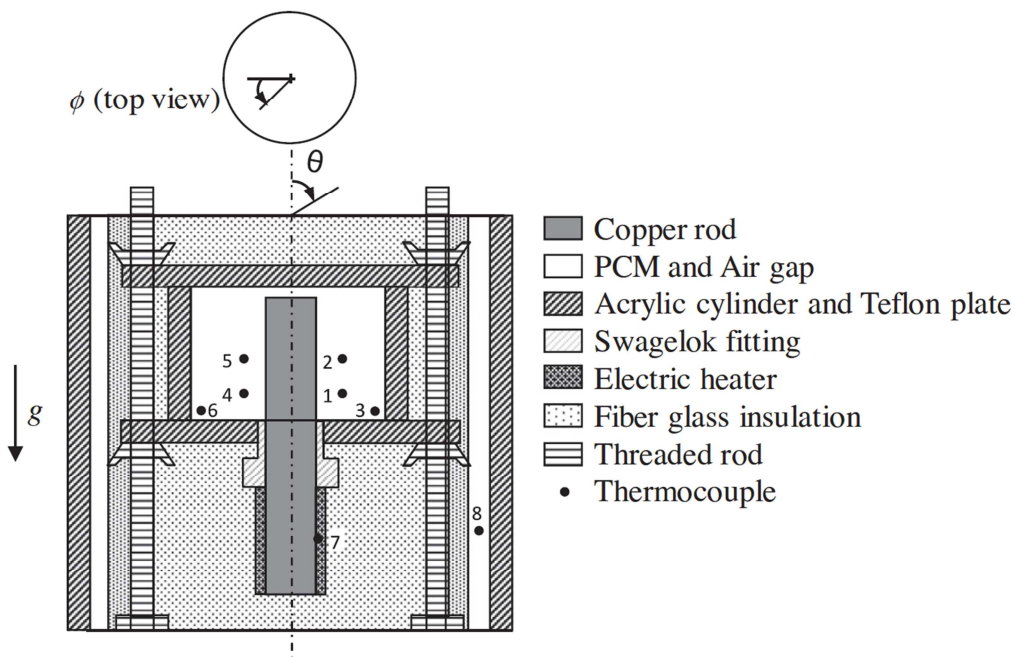

Fig. 3. Schematic of the experimental apparatus

The experiments begin with solid, nearly isothermal PCM that is made free of voids to the extent possible. Prior to each experiment the PCM was conditioned by melting and heating it under vacuum to remove dissolved gases. Subsequently, the degassed PCM was added to the enclosure in a layer-by-layer manner. Specifically, the liquid PCM was injected through small holes in the top Teflon plate using a syringe, creating an approximately 2 mm thick initial PCM layer. The test cell was then refrigerated to solidify the PCM, after which the injection and freezing process was repeated until the enclosure is filled with solid PCM. The test cell and its contents were allowed to equilibrate to room temperature (≈ 25°C) for approximately 12 h, after which the test cell was secured to the tilting table and insulated. The heater was energized to deliver the specified power at the outset of each experiment. Experimental repeatability was checked by performing all experiments twice. Several experiments were performed without the embedded thermocouples to facilitate photographing the time evolution of the PCM melting process. Specifically, without the thermocouples in place the liquid PCM could be drained from the test cell at predetermined times allowing the solid PCM to be removed, sectioned, and photographed.

A comparison between the measured (based on the average temperatures of the two experiments) and predicted temperatures (solid line) for the θ = 0° cases is reported in Fig. 4. The agreement is considered to be satisfactory at the lower power levels, and excellent at P_h = 3 W. The time needed to achieve $T_{e,3} = T_{e,6}$ = 5°C is predicted to be t_{cm} = 3250 s for P_h = 3 W, where t_{cm} is the complete melting time and T_e is the excess temperature ($T_e = T - T_{\text{initial}}$). Hence, the measured and predicted complete melting times are in excellent agreement.

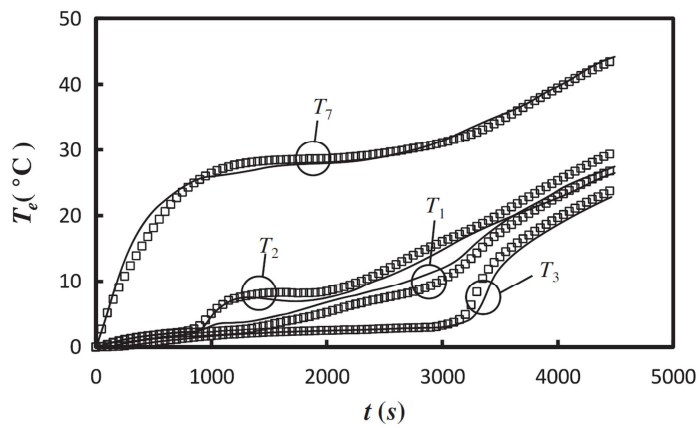

Fig. 4. Predicted and measured temperatures (ϕ = θ = 0°) for input power of P_h = 3 W. Measured values are the averages of Experiments 1 and 2.

Measured temperatures associated with various ϕ and θ = 10°C with P_h = 3 W are shown in Fig. 5. Conditions associated with ϕ = 90° are shown in Fig. 5c (θ = 10°). To orient the reader, the thermocouples associated with T_2 and T_5 are now at the same elevation. However, the thermocouple associated with T_5 is closer to the viewer than the one associated with T_2. As expected, the thermal responses associated with the open- and filled-symbol data points are nearly identical, even though the flow is three-dimensional. The measured thermal responses associated with intermediate values of

ϕ are shown in Fig. 5b and Fig. 5d. In Fig. 5b, the thermocouple associated with T_5 is above and closer to the viewer relative to the thermocouple associated with T_2 whereas in Fig. 5d, T_2 is above T_5, and T_5 is closer than T_2. As expected, the thermal responses of the open-symbol temperatures of Fig. 5b are nearly the same as the responses of the filled-symbol temperatures of Fig. 5d since the open and closed-symbol thermocouples have, in essence, switched positions. The thermal responses of the ϕ = 45° and 135° cases are substantially different than for the ϕ = 0° and 90° cases, again reflecting the three-dimensional nature of the flow and heat transfer within the PCM.

Measured temperatures and observations of the solid–liquid interface show that, for the system considered here, strong 3D effects become apparent even at modest (θ ≈ 5°) tilt angles. Because a 2D numerical model has been used to predict the melting response of the non-tilted experiments, with good agreement between model predictions and experimental measurement, a model based on similar, three-dimensional physical descriptions could be validated using the three-dimensional experimental results reported here. Temperature measurement, visualization of the solid PCM, and visualization and/or measurement of flow conditions within the molten PCM could be performed more easily with use of a larger test cell. Moreover, conjugate effects would become less pronounced in a larger experimental apparatus. However, the natural convection within the molten PCM could involve a transition from laminar to turbulent conditions if a larger test cell were to be used. Larger scale experiments would, therefore, potentially provide data to validate three-dimensional melting models for PCM melting with turbulent free convection in the molten phase.

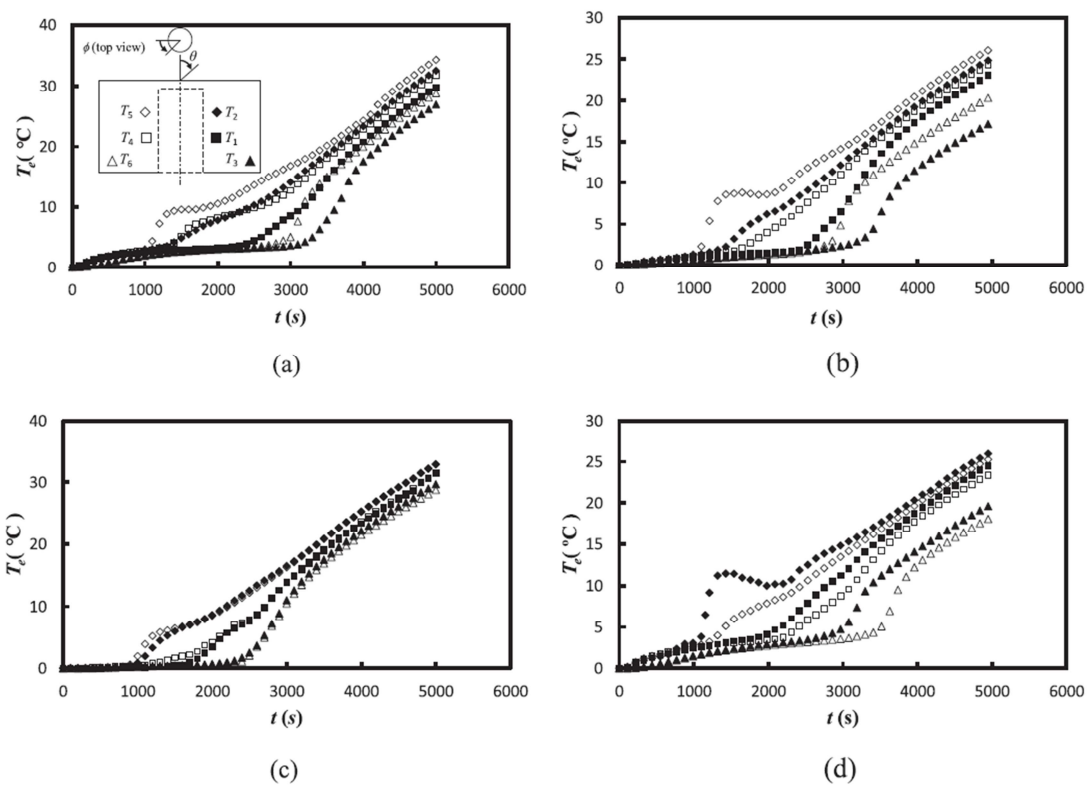

Fig. 5. Measured temperatures for P_h = 3 W, θ = 10°: (a) ϕ = 0°, (b) ϕ = 45°, (c) ϕ = 90°, (d) ϕ = 135°.

System Level Modeling:

Shabgard et al. [62] investigated the effect of adding HPs to a LHTES system using a system level model comprised of a network of thermal elements characterized by a thermal resistance and a thermal capacitance. Two storage configurations were considered; one with PCM surrounding a tube that conveys the heat transfer fluid (Fig. 6a), and the second with the PCM contained within a tube over which the heat transfer fluid flows (Fig. 6b). Both melting and solidification were simulated. It was demonstrated that adding heat pipes enhances thermal performance, which was quantified in terms of dimensionless heat pipe effectiveness.

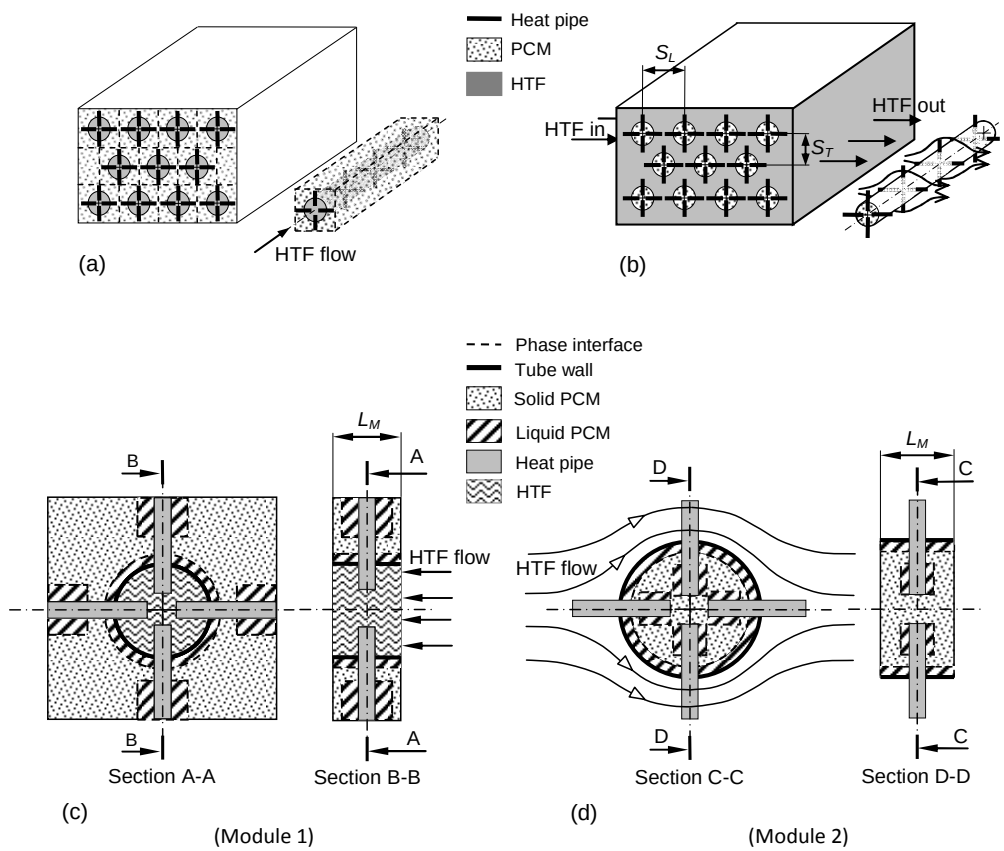

Fig. 6. Two LHTES units: (a) the PCM surrounds the HTF tubes, (b) the HTF passes over tubes containing PCM, (c) Module 1 and (d) Module 2.

The thermal network approach is taken and the network is shown in Fig. 7. Thermal energy is transferred between the HTF (at T_{HTF}) and the solid–liquid interface of the PCM (at T_m). Heat can be transmitted through the HPs, through the HTF tube wall, and through either solid or liquid PCM. Because the transient response of the system is of interest, the thermal network consists of coupled thermal elements, each of which describes both the thermal resistance and the thermal capacitance associated with the element. A system of ordinary first order differential equations is formed by applying the energy balance to each thermal element. The temperatures and heat transfer rates at any time step are solved by solving the above set of governing equations using a Runge–Kutta method. As shown in Fig. 8, heat transfer

enhancements of respectively 60% and 40% could be achieved by using four heat pipes during charging and discharging of either module.

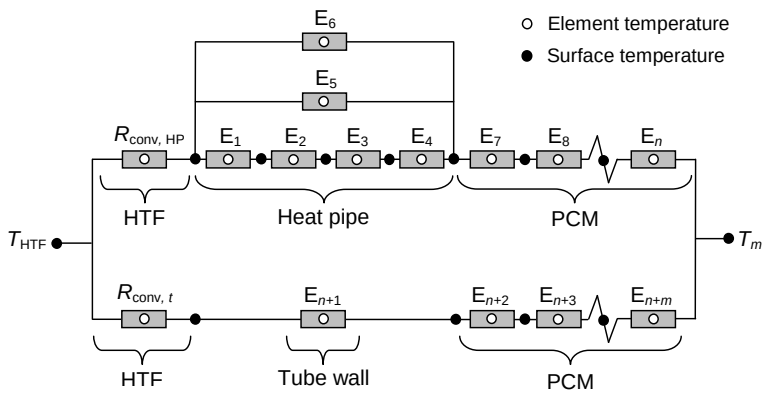

Fig. 7. The thermal network.

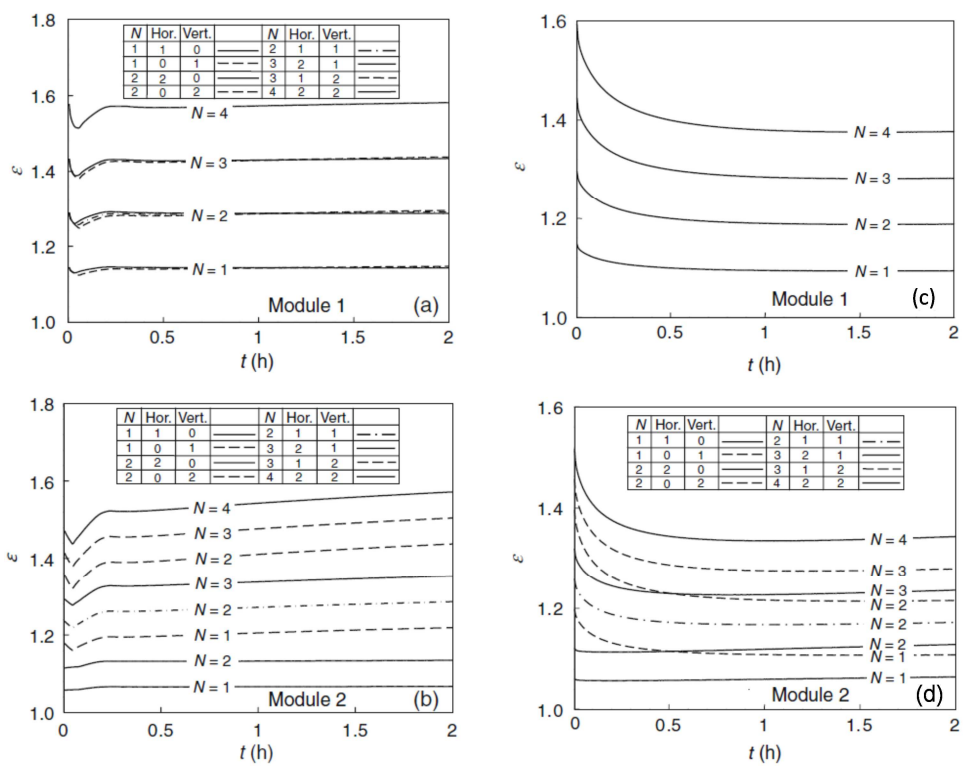

Fig. 8. Heat pipe effectiveness various numbers and orientations of HPs and LM = 0.12 m: (a) charging of Module 1, (b) charging of Module 2, (c) discharging of Module 1, and (d) discharging of Module 2.

It is important to understand the dynamic thermal behavior of the LHTES with embedded heat pipes in order to design the storage system for a CSP plant operation. To this end, a transient numerical model of the large scale HP-TES system is developed and the influence of the design and operating parameters on the dynamic charge and discharge performance of the system is analyzed to identify operating windows that satisfy the SunShot Initiative targets. Based on the parametric studies and specified

constraints on the minimum exergetic efficiency, maximum storage capital cost and minimum discharge time, operating windows are identified on the HTF flow velocity as a function of the various design parameters for non-cascaded and cascaded HP-TES system configurations.

The HP-assisted LHTES system configuration considered in the present model is shown in Fig. 9a. The HTF flow to the storage system is divided equally among the N_d channels where the heat transfer between the HTF and PCM takes place. The schematic of one channel of the heat pipes embedded LHTES system, accompanied by a PCM unit, is also shown in Fig. 9a. As observed from the front view of the channel in Fig. 9b, the height of the channel is represented as H_d, length of the system is represented as L_d while the height of the PCM section is represented as H_p. During charging, hot HTF enters the bottom channel from the left at x = 0 m (Fig. 9b) transferring heat to the PCM through the bottom channel wall and heat pipes while cold HTF during discharging enters the top channel from the right at $x = L_d$ (Fig. 9b). The channel width is denoted by W_d, as shown in the side view (Fig. 9c). The air gap is provided to accommodate the volumetric expansion of the PCM during melting. A top view of a channel in a HP-TES system showing the arrangement of heat pipes along the channel length and across the channel width, W_d, is depicted in Fig. 9d. The transverse pitch, S_T, in Fig. 9d represents the spacing between adjacent heat pipes across the channel width while the longitudinal pitch S_L in Fig. 9b represents the spacing between adjacent heat pipes along the channel length. The arrangement of the heat pipes is staggered in the form of an equilateral triangle.

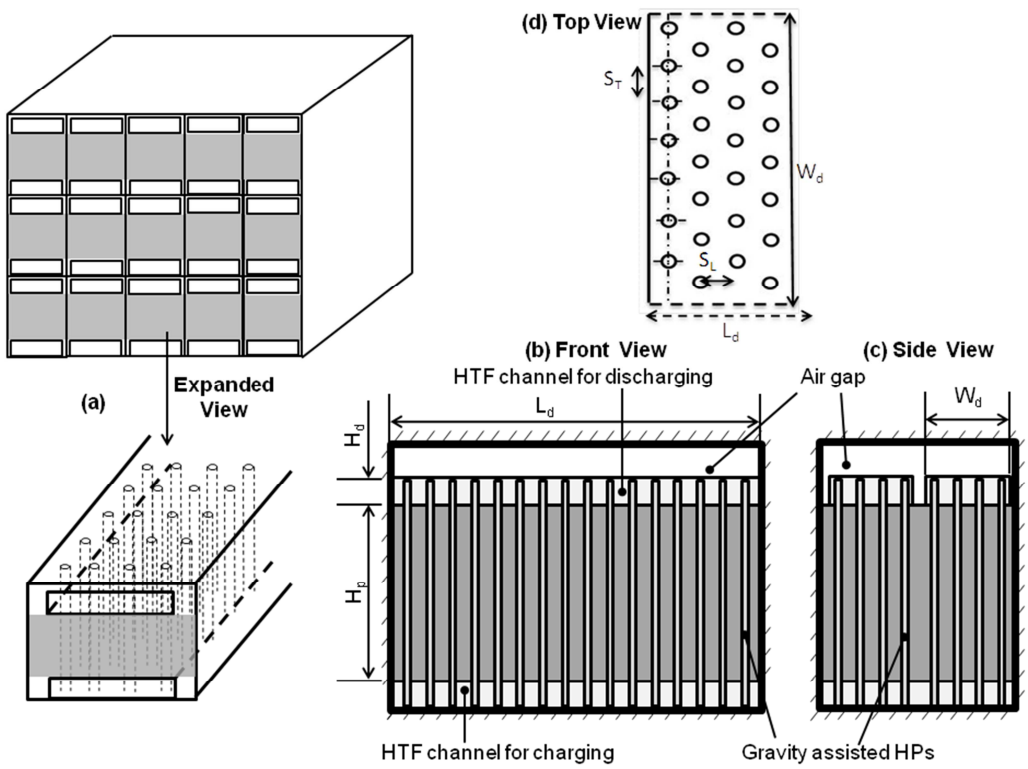

Fig. 9. Schematic illustration of: (a) gravity heat pipes embedded latent thermal energy storage system (HP-TES) and an expanded view of HP-TES channel, and (b) front, (c) side and (d) top view of HP-TES channel.

Sodium-Stainless steel heat pipe is used for the present analysis while solar salt (60 wt. % $NaNO_3$ and 40 wt. % KNO_3) is used as the HTF. The key PCM property parameter that is considered in this study is the melt temperature of PCM. The other design parameters that are considered in this study are the longitudinal spacing between the heat pipes, length, width and height of the channel, the condenser and evaporator length of the heat pipes. The default PCM thermophysical properties chosen for this study are in par with the molten salt PCM values reported in the literature [63]. The HTF flow velocity through a single channel, U_f is the operating parameter considered in the study, the default value of which is taken as 2.53 mm/s.

A cost model is also developed for the HP-LHTES system. The storage cost, α, is calculated for integration of the HP-TES system with a 115 MW_e (270.58 MW_t) power plant operation, corresponding to which the mass flow rate required to meet the design thermal power output is $\dot{m}_d = 635.18\ kg/s$. The capital cost of HP-LHTES system can be expressed as the summation of storage material cost (HTF and PCM), container cost, heat pipes cost and the overhead cost. The storage cost of the HP-LHTES system in $/kWh$_t$ can then be computed as the ratio between the capital cost and storage capacity. The storage capacity of the HP-LHTES system in kWh_t is calculated. The overhead cost, accounting for the miscellaneous costs such as electrical, instrumental, piping, valves and fitting costs is assumed to be 10% of the storage material, container and heat pipes cost. The unit cost of a heat pipe with a sintered metal powder wick is obtained from Ref. [64] to be $5 for total of 100 heat pipes and is available at a discounted pricing for quantities greater than that. Also, the gravity assisted heat pipes only require simple screen mesh wicks for which the cost is even lower and a unit cost (C_{HP}) of $3, similar to that of thermosyphon cost [65] is assumed in the present analysis. The LHTES container cost encompasses the material cost of the stainless steel (321 SS), foundation cost and the insulation cost. The cost per kg of stainless steel is obtained to be $5.43/kg from [66], the calcium silicate insulation cost is assumed to be $235/m^2 [67], and the foundation cost is taken as $1,210/m^2 [68]. The height of the storage system, H_t (Fig. 9) is taken as 20 m, and the storage width W_t, required to accommodate the N_d channels can be calculated from the dimensions of the channel considered. The HTF channel cost comprises the material and the welding cost. Employing the above cost rates, for a two-tank molten salt thermal storage system shows a total cost of $26.72/kWh$_t$, which comes close to the $26.22/kWh$_t$ value reported in Ref. [69].

The model outputs include the spatial, temporal variation of the HTF and PCM temperature; spatial and temporal variation of the melt fraction within the PCM. The key performance metrics analyzed in the present study are the steady state discharge time, t_D [h], storage capital cost per unit thermal energy, α [$/kWh$_t$], and the steady state exergetic efficiency, ζ. The exergetic efficiency of the storage system is defined as the ratio of exergy change of the HTF during discharge t that during charging. An ambient temperature of T_{ref} = 300 K is considered.

Table 1 lists the parameter combinations that maximize the discharge time and exergetic efficiency and minimizes the storage cost, provided the U.S. Department of Energy SunShot requirements are satisfied. For all the channel lengths, the maximum discharge time is obtained for the largest evaporator length of L_e = 0.25 m considered in the present study (Table 1a1) with the rest of the parameters at the default values. As

observed from Table 1, the HTF flow velocity corresponding to the best design point increases with increase in channel length. The number of channels, N_d required to achieve the HTF flow velocity corresponding to the design mass flow rate of 635.18 kg/s for 115 MW_e CSP plant capacity decreases with increase in channel length as tabulated in Table 1a1. The longest discharge time is obtained for channel length of 40 m, t_D = 6.97 h (Table 1a1). Parametric studies of 2-PCM cascaded configurations reveal that the best design configuration depends on the optimal length fractions of each PCM zone and the design that yielded the highest discharge time required a higher fraction of the channel length filled with PCM of high melt temperature. The best design configuration with highest discharge time of t_D = 6.94 h for the 2-PCM cascaded HP-TES system requires that the left and right zones filled with high and low melt temperature PCM, respectively be split in the ratio of 0.9:0.1 (Table 1a2 for L_d = 40 m). The best design configuration for maximum exergetic efficiency (Table 1b) shows that non-cascaded PCM configuration yielded the highest exergetic efficiency.

Table 1. Optimum design obtained from operating windows.

Objective			T_d [C]	L'	H_d [m]	W_d [m]	S_L [m]	L_e [m]	L_c [m]	t_D [h]	U_f [mm/s]	N_d	α [$/kWh$_t$]	ζ [%]
a. Maximum Discharge Time, t_D [h]														
1. 1-PCM (Non-Cascaded)	L_d = 20 m	-	503.0	-	0.250	0.800	0.040	0.250	0.800	6.835	1.270	1266	14.614	95.00
	L_d = 30 m	-	503.0	-	0.250	0.800	0.040	0.250	0.800	6.862	1.905	844	14.934	95.00
	L_d = 40 m	-	503.0	-	0.250	0.800	0.040	0.250	0.800	**6.973**	2.202	731	14.955	95.14
2. 2-PCM (Cascaded)	L_d = 20 m	Top Bottom	503.0 361.0	0.900 1.000	0.250	0.800	0.040	0.200	0.800	6.755	1.230	1308	**14.574**	95.00
	L_d = 30 m	Top Bottom	503.0 361.0	0.900 1.000	0.250	0.800	0.040	0.200	0.800	6.851	1.448	1111	14.716	95.00
	L_d = 40 m	Top Bottom	503.0 361.0	0.900 1.000	0.250	0.800	0.040	0.200	0.800	**6.936**	2.123	758	14.894	95.00
b. Maximum Exergetic Efficiency ζ, [%]														
1. 1-PCM (Non-Cascaded)	L_d = 20 m	-	503.0	-	0.250	0.800	0.040	0.200	1.600	6.167	2.531	636	14.531	96.68
	L_d = 30 m	-	500.2	-	0.250	0.800	0.040	0.200	0.800	6.317	2.531	636	14.856	**97.39**
	L_d = 40 m		503.0	-	0.250	0.800	0.040	0.100	0.800	6.500	2.531	636	14.810	96.64
2. 2-PCM (Cascaded)	L_d = 20 m	Top Bottom	503.0 361.0	0.900 1.000	0.250	0.800	0.040	0.200	0.800	6.750	1.825	881	14.614	96.09
	L_d = 30 m	Top Bottom	503.0 361.0	0.900 1.000	0.250	0.800	0.040	0.200	0.800	6.600	2.907	554	14.886	**96.59**
	L_d = 40 m	Top Bottom	503.0 361.0	0.900 0.100	0.250	0.800	0.040	0.200	0.800	6.900	4.643	347	14.966	96.14
c. Minimum Storage Cost, α [$/kWh$_t$]														
1. 1-PCM (Non-Cascaded)	L_d = 20 m	-	503.0	-	0.250	0.800	0.040	0.200	1.600	6.167	2.531	636	**10.319**	95.00
	L_d = 30 m	-	503.0	-	0.250	0.800	0.040	0.200	1.600	6.638	2.857	563	10.718	95.00
	L_d = 40 m		503.0	-	0.250	0.800	0.040	0.200	1.600	6.400	4.067	396	10.851	95.00
2. 2-PCM (Cascaded)	L_d = 20 m	Top Bottom	503.0 361.0	0.900 1.000	0.250	0.800	0.040	0.200	0.800	6.750	1.230	1308	**14.574**	95.00
	L_d = 30 m	Top Bottom	503.0 36100	0.900 1.000	0.250	0.800	0.040	0.200	0.800	6.600	1.448	1111	14.716	95.00
	L_d = 40 m	Top Bottom	503.0 361.0	0.900 1.000	0.250	0.800	0.040	0.200	0.800	6.283	2.123	758	14.894	95.00

The maximum exergetic efficiency is obtained for an intermediate channel length of 30 m for both non-cascaded and 2-PCM cascaded configuration. The highest exergetic efficiency of $\zeta = 97.39\%$ is obtained for a non-cascaded HP-TES system with channel length, L_d = 30 m and filled with PCM melting at 500.16°C, which is the discharge cut-off temperature. Although the design configurations that yield the maximum exergetic efficiency (Table 1b2) are the same as that obtained for maximum discharge time (Table 1a2), the HTF velocity in Table 1b.2 are relatively higher than that obtained in Table 1b1 for maximum discharge time. For instance, for the channel length of 30 m in Table 1b2, the highest exergetic efficiency is obtained for a HTF flow velocity of 2.91 mm/s while the highest discharge time for the same channel length in Table 1a2 is obtained for U_f = 2.12 mm/s. The lowest storage cost for non-PCM cascaded

configuration is obtained for a condenser length of 1.6 m and channel length of 20 m, \$10.32/kWh$_t$ (Table 1c1) due to increase in storage capacity as a result of increase in PCM volume with increase in L_c.

Besides the analysis of LHTES system, the performance assessment of concentrating solar plants (CSP) integrated with thermal energy storage system is crucial to ascertain the role of LHTES systems in reducing the levelized cost of electricity. As a part of the project, the influence of design parameters of the storage system on the performance of a power tower CSP plant is studied to establish design envelopes that satisfy the U.S. Department of Energy SunShot Initiative requirements. A schematic of the integration of the LHTES in a power tower CSP plant working on s-CO_2-Brayton cycle is shown in Fig. 10 for a typical discharge operation. A power tower CSP plant comprises of five sub-systems namely, the heliostat field, central tower/receiver, power block, cooling tower and TES system. In the external tower/receiver, molten salt HTF is circulated to absorb the solar thermal energy reflected by the heliostats. The hot HTF exiting the receiver is then fed into the power block to convert the thermal energy into electrical energy with a rated cycle conversion efficiency of 41.6% and 53.8% for the Rankine and the s-CO_2 cycles, respectively [70]. The inlet temperature and pressure of the steam at the inlet of the turbine are typically 574°C and 100 bar, respectively, while those for the s-CO_2 cycle in Fig. 10 are 850°C and 20 MPa, respectively. The hot steam/s-CO_2 from the turbine exit is fed into a condenser/cooling tower to condense the exhaust steam by rejecting the heat of vaporization to the cooling medium as illustrated in Fig. 10. A dry cooling technology is considered in the present study instead of the conventional wet cooling tower owing to high water consumption in spite of the improved performance and lower cost.

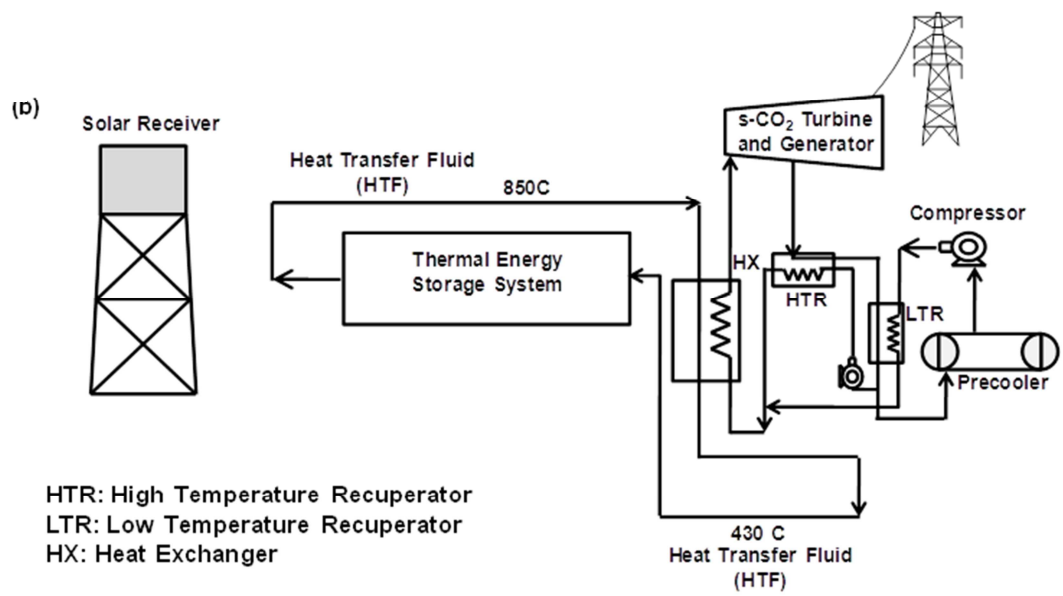

Fig. 10. Schematic illustration of concentrating solar power (CSP) plant integrated with thermal storage system working on supercritical carbon-dioxide (s-CO2) cycle.

A “process-based” approach, in which a system is modeled from the ”bottom up“ using component masses and process energy flows is implemented in the present

study. The dynamic model uses actual weather data at time intervals of one hour and calculates the net electrical energy output at every time step during an entire year, thus simulating the hourly, monthly and annual energy output of a solar thermal power plant. The power block component calculates the net Rankine cycle conversion efficiency, expressed as a function of the inlet temperature and mass flow rate of the HTF from the solar field and the ambient temperature, thus properly accounting for the reduction in efficiency during part load conditions. The expression for Rankine cycle efficiency is obtained based on the parametric studies of various operating conditions using a high-fidelity process model.

The complete formulation, including the CSP plant performance model, the storage performance model and the cost model, was implemented in FORTRAN. The model is validated with the results from SAM [71] for a CSP plant with no storage and for a CSP plant with 6 hours of 2-tank direct molten salt storage system. It is to be noted that the outputs from SAM have been validated with experimental results obtained from the operation of Solar II CSP plant installed in Daggett, CA. The major inputs for the CSP plant performance model include the weather data of the location, design parameters of the heliostat, receivers, type of cooling tower, power plant output requirement to name a few. The models assume a plant life of 30 years and the geographic location used is Daggett, CA, where the annual DNI is among the highest in the U.S. The HTF used in the CSP plant integrated with Rankine power cycle corresponds to 60% $NaNO_3$-40%KNO_3 (Solar Salt) [69] while that used in CSP plant integrated with s-CO2 power cycle corresponds to KCl-$MgCl_2$ [72].

A 2-PCM cascaded storage system is assumed, with 75% of the total channel length from the hot HTF inlet (Fig. 10) filled with PCM of high melt temperature while the remaining 25% of the volume filled with PCM of low melt temperature. The high melt temperature PCM chosen for this study corresponds to a blend of Li_2CO_3(35%) and Na_2CO_3(65%) for low temperature Rankine based CSP plant while for the high temperature s-CO_2 based Brayton cycle operation, a blend of K_2CO_3(51%)–Na_2CO_3(49%) is chosen. The low temperature PCM for both the configurations is chosen as Li_2CO_3(32%)–K_2CO_3(35%)–Na_2CO_3(33%). The operating parameters namely, HTF inlet mass flow rate and HTF inlet temperature depend on the hour of the day, available solar insolation, etc., is dictated by the CSP plant operation. The influence of HTF channel width (W_d), channel length (L_d) and the longitudinal spacing between the heat pipes (S_L) are the major design parameters of the HP-TES system considered in the present study.

The major outputs from the model are the hourly net and gross electric power output, hourly inlet temperature of the power block, hourly inlet temperature and mass flow rate of the LTES system, hourly exergy input and output of the LTES system. The key performance metrics characterizing the performance of the CSP plant integrated with storage system are the plant capacity factor, β, annual exergy efficiency of the LTES and the levelized cost of electricity (LCE). The capacity factor (β) of a power plant is the ratio of the actual output of a power plant over a period of time and its output if it had operated at full nameplate capacity the entire time while the levelized cost of electricity is calculated according to [71]. The total installed costs of 200 MW_e power tower CSP plant without storage as reported in Ref. [71] for Rankine cycle based and s-

CO_2 based power block are \$5,672.30/kW$_e$ and \$3,330.90/kW$_e$ to which the storage capital cost is added to obtain the total installed cost of the plant.

The corresponding combinations of the optimum design parameters and the performance metrics are tabulated in Table 2 and Table 3. Table 3 also shows the sensitivity of the LCE to the heat pipe cost. In addition to that, these tables compare the impact of the storage system on the LCE of 200 MW$_e$ CSP plant working on a Rankine cycle and s-CO_2 cycle integrated with 2-tank molten salt storage system. For the solar multiple of 2.7, minimum LCE of 6.45 ¢/kWh is obtained for a 2-tank sensible energy storage system of radius, 18.5 m (Table 2), which is relatively higher than that obtained for HP- TES, LCE = 5.77 ¢/kWh due to lower storage capital cost of HP-TES and higher storage capacity of HP-TES. The minimum LCE for HP-TES system is obtained for a longitudinal spacing of 3.3 cm with a total of 15.62 million heat pipes (Table 3(i)). The maximum unit cost of heat pipes beyond which the LCE exceeds the 6 ¢/kWh target corresponds to \$4/unit HP (Table 3(ii)). For a Rankine cycle based CSP plant, a longer channel height and width embedded with a total of 24.9 million heat pipes is required to achieve the least LCE of 9.69 ¢/kWh (Table 3(i)). Compared to the minimum LCE obtained for s-CO_2 based CSP plant operation integrated with 2-tank molten salt storage system (Table 2), the LCE of the HP-TES system is at least 0.68 ¢/kWh less (Table 3(i)).

Table 2. Optimum 2-tank design configuration for least LCE.

Power Plant Cycle	Storage Type	Tank Radius, R_t [m]	Tank Height, H_t [m]	Annual Net Electric Output Q_e, [GWh]	Capacity Factor, β [%]	Storage Capital Cost, α [US\$ MM]	LCE [¢/kWh]
s-CO_2	No TES	-	-	553.5	31.6	-	11.07
	2-Tank	*17.2*	*20*	*1118.9*	*65.4*	*158.1*	*6.45*
Rankine	No TES	-	-	565.5	32.3	-	17.46
	2-Tank	23.7	20	1160.3	66.2	204.6	9.92

Table 3. Optimum HP-TES system design configuration for least LCE

Power Plant Cycle	Heat Pipe Cost [\$/unit]	Channel Length, L_d [m]	Channel Width, W_d [m]	Longitudinal Spacing, S_L [cm] (No. of HPs)	Annual Net Electric Output, Q_e [GWh]	Exergetic Efficiency, ζ [%]	LCE [¢/kW]	Storage Capital Cost, α [US\$ MM]
s-CO_2	(i) *2.0*	*25*	*1.2*	*3.3 (15,624,164)*	*1158.7*	*97.05*	*5.77*	*78.61*
	(ii) 4.0	*25*	*1.2*	*3.3 (15,624,164)*	*1158.7*	*97.05*	*6.05*	*110.5*
Rankine	(i) 2.0	30	1.6	3.3 (24,898,663)	1122.1	97.61	9.69	124.7
	(ii) 4.0	25	1.2	3.3 (24,898,663)	1122.1	97.61	10.05	175.7

Although the potential of LHTES systems to reduce the cost of solar electricity generation has been stressed by several investigators, to the authors' knowledge it has not been shown how this approach could be implemented at a scale commensurate with CSP. The incorporation of gravity-assisted wickless heat pipes (thermosyphons) in a large scale LHTES system for commercial CSP was studied by Robak et al. [65]. A LHTES system design is proposed which can operate effectively during a charging and discharging period. A heat transfer model is utilized to estimate, for example, the size and number of thermosyphons needed in the LHTES. An economic evaluation of the system is carried out, and the design is compared with a two-tank SHTES to determine whether LHTES with embedded thermosyphons can be cost-competitive.

The design considered here incorporates thermosyphons to promote heat transfer between the cold HTF and the solid–liquid interface of the hot PCM. As shown in Fig. 11, the LHTES unit might consist of a header (not shown) that partitions the cold HTF into a series of channels within the LHTES unit. Each HTF channel is studded with an array of thermosyphons that span between the HTF and PCM. As such, the HTF channels, along with the thermosyphons, are the surfaces upon which the PCM solidifies. For a given amount of solid PCM, (a) the surface area of the PCMs solid–liquid interface is large compared to the case without thermosyphons, and (b) the mean distance between the cold surfaces and the PCM solid–liquid interface is small, compared to the case without thermosyphons. These dual effects – increased solid–liquid interface area and reduced distances between the solid–liquid interface and the cold HTF surface – will reduce the thermal resistance between the cold HTF and the solidifying PCM. At the LHTES unit exit, a second header (not shown) combines the individual heated HTF streams. During charging, the direction of HTF flow through the LHTES unit is reversed and the HTF is cooled as it melts the PCM. To reiterate, natural convection occurs within the molten PCM that is adjacent to the hot surfaces during LHTES charging, resulting in a low thermal resistance between the HTF and the PCMs solid–liquid interface relative to the conduction-dominated discharging process.

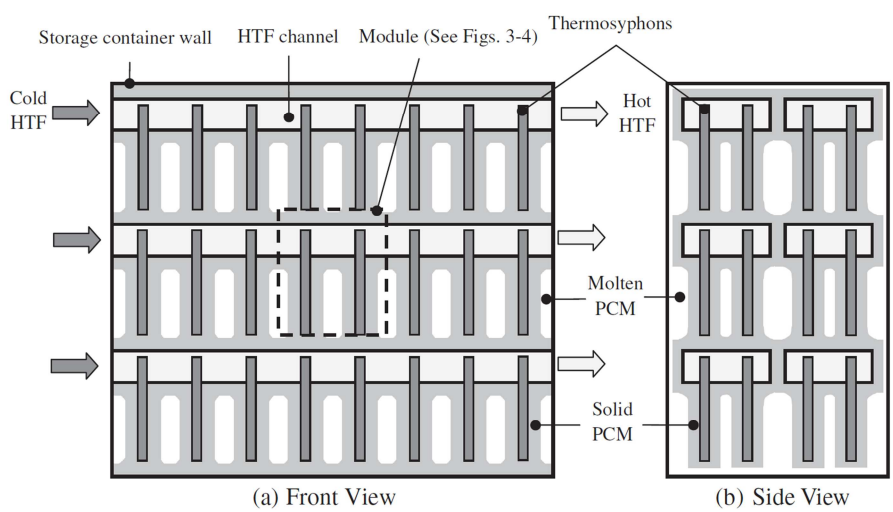

Fig. 11. Cross-sectional views of a LHTES system with embedded thermosyphons during discharging: (a) lengthwise view and (b) widthwise view. The dashed box corresponds to a unit module.

A mixture of LiCl/KCl is selected for this study because its melting temperature (348°C) is approximately midway between the 280°C LHTES HTF inlet temperature specified for modern CSP operation during discharging, and the 390°C HTF coming from the solar field during charging [67]. Shabgard's thermal network model for LHTES with embedded heat pipes [62] was modified and used here. The LHTES system shown in Fig. 11 is composed of a number of unit cells, or modules, such as the one shown by the dashed lines in Fig. 11. A representative module consists of two staggered rows of thermosyphons (into the page) and surrounding PCM, and is centrally-located in the LHTES unit. It is assumed that this module experiences HTF thermal conditions that are the average of the inlet and outlet temperatures, which are specified. The PCM is initially assumed to be liquid at its solidification temperature. The thermosyphons are arranged in staggered rows to minimize the thermal resistance associated with forced convection heat transfer between the HTF and the condenser section of the thermosyphon [62].

The network model [62] is used to determine the heat transfer from the solidifying PCM to the HTF. Included in this calculation (for which potential contact resistances at the solid PCM-metal interfaces are neglected since the main resistance to heat transfer is associated with the low thermal conductivity of the solid PCM) is the time variation of the radius of solid PCM that forms on the condenser sections of the thermosyphons. The network model simulation is curtailed at the specified discharging period. Once the final radius of solid PCM is determined, the number of thermosyphons that can be placed in the two staggered rows of the HTF channel (of specified width) is found using simple geometric arguments. The length (in the direction of HTF flow) of the module can be computed in a similar manner.

In addition to PCM solidification on the thermosyphon condenser sections, the network model computes the thickness of solid PCM that freezes on the four cold HTF channel surfaces. The module width is determined based upon the specified channel width plus twice the thickness of solid PCM around the sides of the HTF channels. The module height is found by adding the thickness of PCM along the top of the HTF channel with thermosyphon overall length, and HTF channel wall thickness. With the module width, length, and height determined, the overall size of the LHTES system can be computed as follows. The total length (in the direction of the HTF flow) of each HTF channel is based upon the heat transferred in one module to the HTF from the solid PCM over the discharging period. Thus, with the mass flow rate of the HTF per module (or channel) specified, along with the HTF properties, the increase of the HTF temperature through a single module can be computed. The number of modules (in the direction of the HTF flow) is then calculated based upon the temperature increase per module and the overall temperature increase over the entire LHTES. Hence, the total length of the LHTES can then be determined. Subsequently, the total number of HTF channels required is determined by calculating the thermal energy storage required of the LHTES unit, based on the specified electric power production of the Rankine cycle, and the efficiency that was determined. Finally, (a) the total size of the LHTES unit is found from knowledge of the total number of HTF channels and (b) the required number of thermosyphons is found from the total number of modules, the module size, the thermosyphon dimensions, and the thickness of the PCM solidified on the thermosyphons over the discharging period.

Once the physical details of the LHTES design are determined, the capital costs of the major components can be estimated based upon their size and mass. Capital costs for the LHTES unit are associated with four main system components: (1) the exterior storage container, (2) the PCM, (3) the thermosyphons, and (4) the internal architecture of the LHTES unit such as the HTF channels. Manufacturing and assembly cost estimates are included in the analysis and are based upon publically-available information (for example, [67,68]). In addition to the costs of the four major system components, a 10% overhead is added to the total capital cost. This overhead covers secondary components such as instrumentation, wiring, piping, valves, and insulation, and matches the rate used in a two-tank SHTES economic analysis [68].

Table 4. Capital costs for LHTES and two-tank SHTES [68]**.**

Equipment	LHTES cost (US$ MM)	SHTES cost (US$ MM)
Energy storage material[a]	14.9	21.0
Storage container	4.8	10.4
Thermosyphons	11.1	–
HTF channels	1.6	–
Molten salt heat exchanger	–	5.4
Molten salt pump	–	1.6
Overhead (10%)	3.3	3.9
Total	35.7	42.3

Table 4 presents a comparison between the estimated capital costs of the LHTES (with thermosyphons) and a SHTES [68] for a 50 MWe unit with 9 h storage (thermosyphon unit cost is coupled to the carbon steel cost for this portion of the study, giving a unit thermosyphon cost of $3.40). Overall, the LHTES system is estimated to have an approximate capital cost of $36 MM, compared with $42 MM for a SHTES system. Most of the savings is associated with reduced expenditures for the energy storage medium and the storage container (Table 4, lines 1 and 2). However, LHTES has two capital costs which do not exist for SHTES; the thermosyphons, and the HTF channels (Table 4, lines 3 and 4). But, the SHTES requires a molten salt-HTF heat exchanger and molten salt pumps ($7 MM, Table 4, lines 5 and 6). In addition the SHTES requires operation of salt pumps (550 kW), meaning SHTES has an additional operating cost relative to LHTES [68]. In total, the economic calculations suggest that at least 15% capital cost savings over SHTES can be realized using an LHTES design.

Fig. 12 shows the dependence of the LHTES cost on the HTF channel height, HTF channel width, and HTF flow rate per HTF channel. As the height of the HTF channel, H_{chan}, is increased with all other parameters held at their base case values (Fig. 12a), the capital cost of the LHTES system increases modestly, whereas when the width of the channel, W_{chan}, is increased with all other parameters at their base case values (Fig. 12b) the cost decreases. Therefore, it is concluded that HTF channels with $W_{chan} / H_{chan} > 1$ are desirable. In essence, large, flat HTF channels provide more area for insertion of thermosyphons. From the parametric study, it is found that HTF channels of approximately 0.08 m in height and 1 m in width (identified as open symbols in the figures; the same as the base case values) lead to desirable performance and cost competitiveness. The HTF mass flow rate per channel also impacts the capital cost of

the LHTES. Fig. 12c shows the sensitivity of the capital cost for the proposed LHTES design to the HTF mass flow rate, with all other parameters at their base case values. High mass flow rates correspond to smaller increases in the HTF fluid temperature per unit HTF channel length and, in turn, longer storage tanks. This increases storage container and storage foundation costs. On the other hand, lower HTF flow rates lead to shorter, more numerous HTF channels which can be stacked in the vertical direction, reducing the overall cost. Again, the base case value is identified as the open symbol.

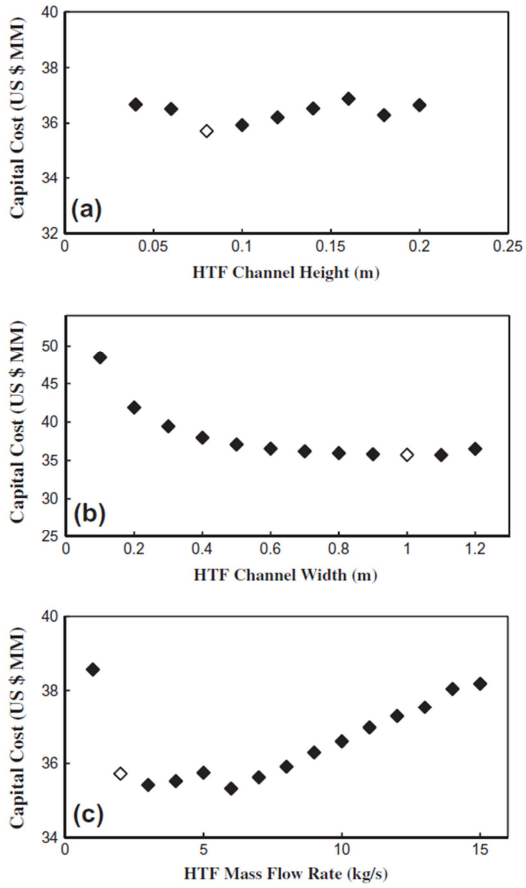

Fig. 12. LHTES capital cost dependence on (a) HTF channel height, (b) HTF channel width, and (c) HTF mass flow rate. The white diamonds represent base case conditions.

The thermal network approach developed in [62] was extended by Shabgard et al. [73] and was employed to predict the performance of latent heat thermal energy storage (LHTES) systems including cascaded phase change materials (PCMs) and embedded heat pipes/thermosyphons. Because the design of LHTES systems involves a compromise between the amount of energy stored, the heat transfer rate, and the quality of the released thermal energy, an exergy analysis is also carried out to identify the preferred LHTES design. It is found that the LHTES with the lowest melting temperature PCM yields the highest exergy efficiency. However, a cascaded LHTES recovers the largest amount of exergy during a 24 h charging–discharging cycle. Quantitatively, the cascaded LHTES recovers about 10% more exergy during a 24 h charging–discharging cycle compared to the best non-cascaded LHTES considered in this work.

A LHTES system with three individual PCM units is considered in which solar thermal energy is stored in the PCMs during charging, and recovered (to operate a power cycle) during discharging (see Fig. 13). The HTF that leaves the LHTES during charging returns to the collector field. The output HTF of the LHTES during discharging is the heat source of a power cycle (not shown). Hence, each PCM unit contains a single PCM. The PCM units also act as heat exchangers, transferring thermal energy between the HTF and the PCM during the charging and discharging cycles. As shown in Fig. 14 and Fig. 15, the PCM in each unit (which is taken to be 20 m long) is housed between HTF flow channels located at the top and bottom of a rectangular container. Multiple gravity-assisted heat pipes, with their ends penetrating into the HTF channels, pass through the PCM in each unit (for brevity, the gravity-assisted heat pipes will also be referred to as heat pipes from now on). The three PCM units can have various depths to provide the desired storage capacity; hence multiple flow channels can exist in each PCM unit for purposes of illustration, only two channels are shown on top of the PCM unit in the side views of Fig. 14 and Fig. 15. The air gap above the PCM is intended to accommodate the expansion of the PCM during melting, and the outer surfaces of the PCM units are insulated. The heat pipes are assumed to be installed in a staggered arrangement. The thermal energy pathways during charging and discharging modes are shown in Fig. 14 and Fig. 15, respectively.

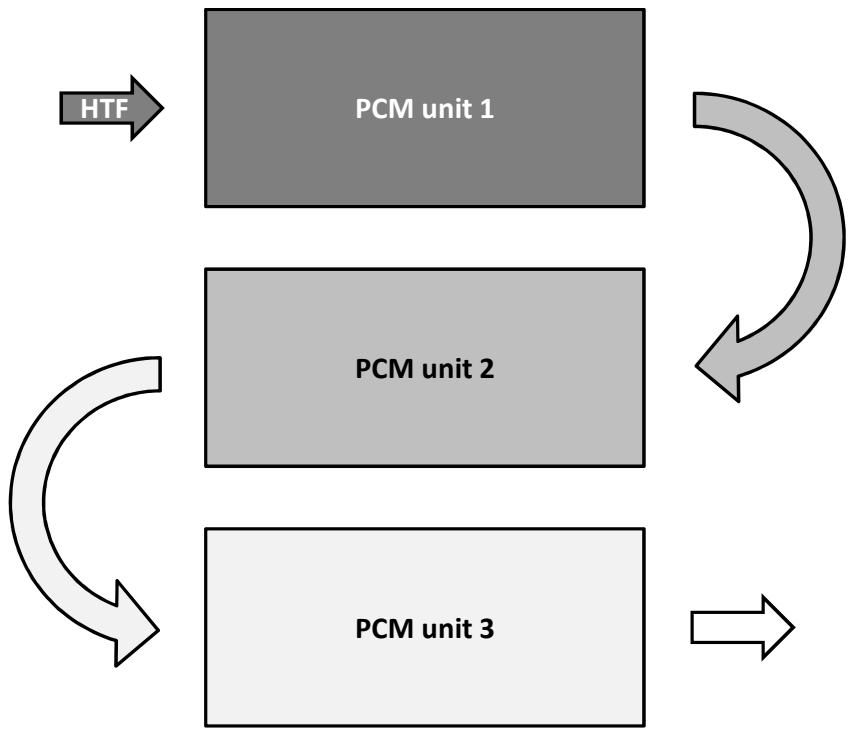

Fig. 13. Cascaded LHTES consisting of three PCM units.

The heat transfer model predicts heat transfer and phase change rates, as well as HTF outlet and PCM temperatures. However, LHTES systems characterized by high heat transfer rates during charging may experience low heat transfer rates during discharging, or vice versa. Hence, it is difficult to identify the preferred LHTES system based upon a heat transfer analysis alone. To assist in the performance evaluation an

exergy analysis is performed to serve as a complementary tool to identify the preferred LHTES system, based on a judicious compromise between the amount of thermal energy recovered, and the quality (i.e. temperature) of the delivered thermal energy. The second-law comparison is facilitated by defining an appropriate exergy efficiency, and comparing various LHTES systems in terms of that efficiency [33,34,36,37]. The exergy efficiency, ε, is defined as the ratio of exergy recovered by the HTF during discharging to the total exergy content of the HTF at the inlet of the LHTES during charging [34]. The properties of the PCMs considered in this work are listed in Table 5. Representative inlet HTF temperatures during charging and discharging of 390°C and 280°C, respectively, are specified along with a HTF mass flow rate of 3 kg/s per each channel.

Table 5. Properties of the PCMs

PCM composition (wt %)	Melting Temp. (°C)	Heat of fusion (kJ/kg)	Density (kg/m^3)	Thermal conductivity (W/m·K)	Specific heat (kJ/kg·K)
1; NaOH–NaCl(26.7),	370	370	1960	0.79	1850
2; KCl(22.9), $MnCl_2$(60.6), NaCl(16.5) [63]	350	215	2250	0.95	960
3; NaOH(65.2), NaCl(20), Na_2CO_3(14.8) [63]	318	290	2000	1.0	1850

Thermal energy stored and recovered, as well as the duration of a complete charging-discharging cycle for charging periods of 8 h and 12 h are shown in Fig. 16. In each case, the charging process is, in general, characterized by 3 stages. Initially, heat transfer to the solid PCM is conduction-dominated, with maximum heat transfer rates occurring at t = 0 h. During the subsequent melting period, natural convection occurs in the molten PCM, and heat transfer rates approach time-independent values. Finally, after most of the PCM is melted, the diminishing temperature differences between the PCM and HTF lead to reduced heat transfer rates. The discharging processes of Fig. 16, in general, are also characterized by three stages. Initially high heat transfer rates occur because natural convection and high temperature differences promote heat transfer between the HTF and the superheated PCM. Subsequently, solid PCM forms on the heat transfer surfaces, increasing the thermal resistance between the HTF and the solid-liquid interface of the PCM, reducing heat transfer rates. Finally smaller heat transfer rates occur during the subcooling of the solid PCM. For either charging duration (8 h or 12 h), LHTES 3 (the LHTES containing PCM 3 in Table 5) provides the greatest amount of heat storage and recovery, but has the longest discharging period. Also, 12 h of charging for LHTES 3 corresponds to an overall cycle duration greater than 24 h, which is impractical. In contrast, LHTES 1 (the LHTES containing PCM 1 in Table 5) provides the smallest amount of energy storage, but has the shortest duration of discharging. The responses of LHTES 2 (the LHTES containing PCM 2 in Table 5) and the cascaded system are bracketed by those of LHTES 1 and 3.

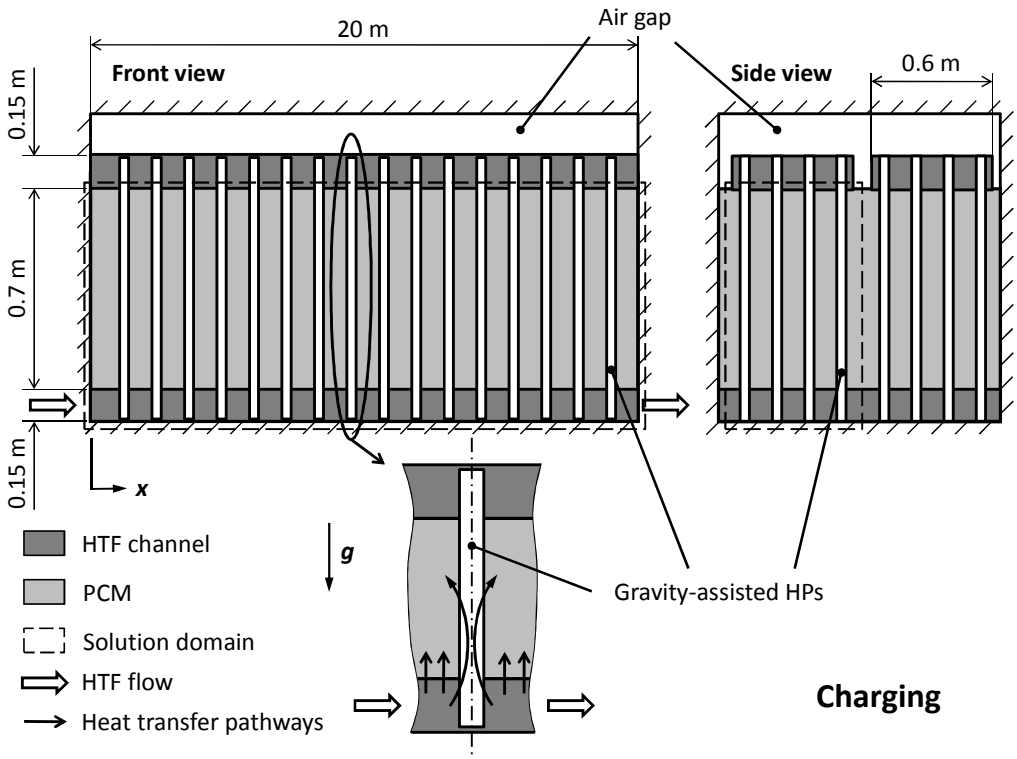

Fig. 14. PCM unit configuration during charging.

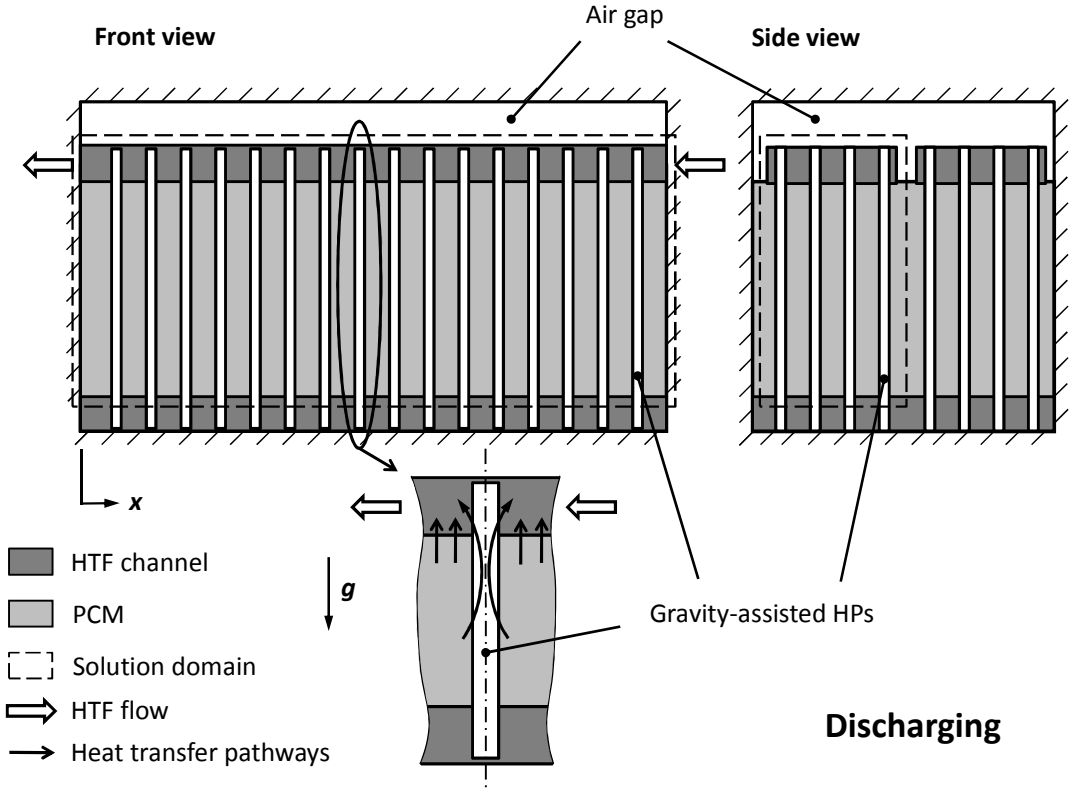

Fig. 15. PCM unit configuration during discharging.

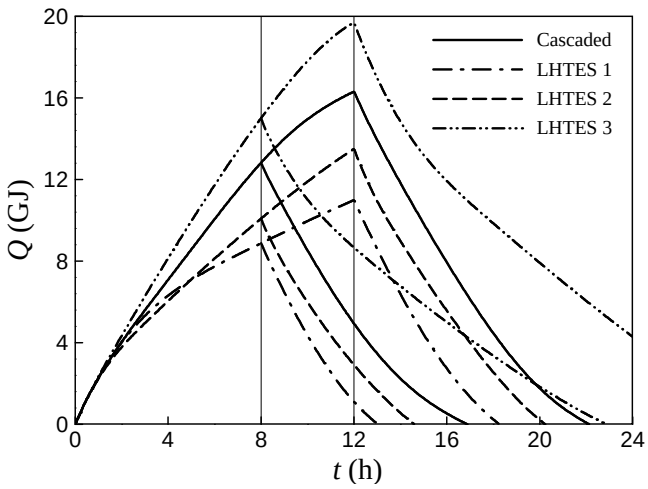

Fig. 16. Energy storage and recovery during charging-discharging cycles with charging periods of 8 and 12 h.

Fig. 17 shows the exergy recovered by the HTF for various charging times. (Overall charging-discharging times would exceed 24 h if any of the curves would be extended to larger t_c.) In practice, it is desirable to maximize the recovered exergy. It is evident that, for t_c δ 10.5 h, LHTES 3 outperforms the other three systems since the exergy recovered by LHTES 3 at its maximum charge time ($t_c \approx 8$ h) exceeds that of any of the other three systems for charging times less than 10.5 h. For t_c τ 10.5, however, the cascaded system yields the highest exergy recovery. The charging time beyond which the cascaded system outperforms LHTES 3 is the critical time, t_{crit}, in Fig. 17 ($t_{crit} \approx 10.5$ h). Hence, the appropriate selection of the LHTES system depends on the location of the CSP plant and the daily availability of solar irradiation.

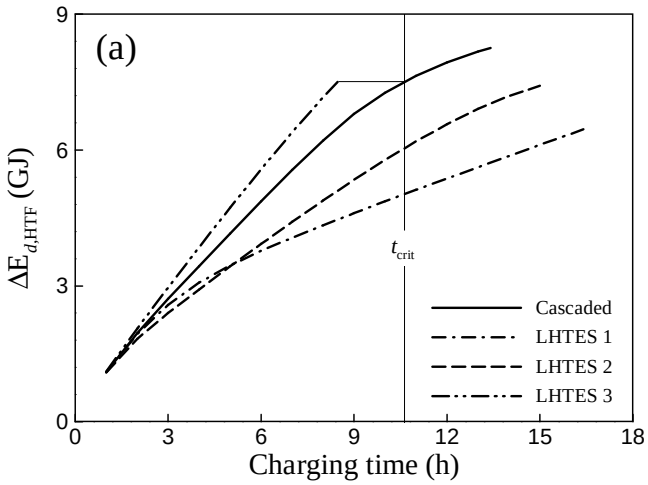

Fig. 17. Variation of total exergy recovered by the HTF, with the charging time.

In order to analyze the performance of LHTES systems in solar applications from a broader perspective, a combined heat transfer and thermodynamic analysis is necessary [74]. Most of the preceding exergy analyses carried out on LHTES systems did not take into consideration the finite duration of the discharge process. Hence, in

some cases optimum LHTES performance corresponds to *infinite* discharging times [36], limiting the practical usefulness of the analyses. Shabgard et al. [75] investigated the optimal design of a LHTES system for solar applications accounting for the finite duration of a charging-discharging cycle. In this study, a combined heat transfer and exergy analysis of a LHTES system for CSP is developed. Two practical constrains, namely (*i*) the equality of the energy stored and recovered and (*ii*) the finite duration of the charging-discharging cycle imposed by the solar day are accounted for. As will become evident, inclusion of these constraints provides guidance in terms of identifying conditions that maximize the exergy extracted from the storage system during the discharge period. It will also be shown that the conditions that maximize the exergy extracted may not be practical, based on the solar availability during the 24 hour day. However, modification of the heat transfer aspects of the LHTES design, such as making use of extended surfaces, can ameliorate this situation, leading to improved system performance.

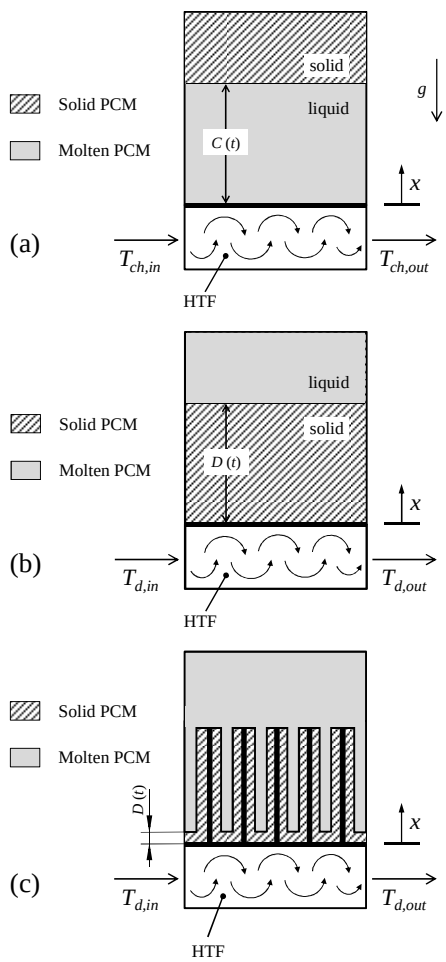

Fig. 18. The LHTES system during (a) charging (A_r = 1), (b) discharging (A_r = 1), and (c) discharging (A_r > 1).

During charging (Fig. 18a) heat is transferred from the warm HTF, through the channel wall, and through the molten PCM by natural convection to the solid-liquid interface located at $C(t)$. During the discharge process (Fig. 18b or Fig. 18c), the PCM

solidifies at $D(t)$ as heat is transferred from the solid-liquid interface, through the solid PCM and channel wall by conduction, to the cool HTF. To enhance heat transfer, extended surfaces could be added to the solid wall and, in the limiting case of an isothermal channel wall (and extended surfaces), solid PCM would form along the entire cold surface, resulting in the solidification process shown in Fig. 18c.

Of interest is the performance of the LHTES system taking into account two practical constraints: (*i*) the equality of the thermal energy stored and recovered, and (*ii*) the maximum 24 hour duration of a complete charging-discharging cycle. As noted previously, only the essential heat transfer processes are accounted for; a more detailed description of the heat transfer phenomena could be included in a more thorough analysis. Specifically, the following assumptions are made.

One-dimensional heat transfer is assumed throughout an entire cycle that consists of an initial charging regime followed by a discharging regime. The HTF and PCM properties are assumed to be constant, and the properties of the solid PCM are taken to be those of the liquid phase. The PCM is a pure (or eutectic) material with a unique phase change temperature, and is solid and at its melting temperature at the beginning of the charging regime. The sensible energy component of the energy storage is taken to be negligible (the Stefan number is zero), and the channel wall (and extended surfaces) is assumed to be comprised of a high thermal conductivity material that poses negligible thermal resistance and has negligible thermal mass. Possible thermal contact resistances and heat losses from the container walls are neglected, and volumetric radiation within the PCM is not accounted for. The rectangular HTF channel is of constant cross-sectional area.

The total dimensionless exergy recovered by the HTF during the discharge process can be found by integrating the rate of the change of the exergy of the HTF during the discharge process with respect to the duration of the discharge regime. An exergy efficiency can be defined by dividing the total exergy recovered during the discharge by the total exergy content of the HTF at the inlet of the LHTES during charging. In general, it is desirable to maximize both the non-dimensional exergy recovery ($\Delta\chi_{\mathrm{HTF},d}$) and the exergy efficiency (ε). As will become evident, however, maximizing both parameters simultaneously is not possible, and we will choose to maximize the exergy recovery.

The exergy recovered during the discharge $\chi(=\Delta\chi_{\mathrm{HTF},d})$, and the exergy efficiency, ε, are reported in Fig. 19 for $\overline{T}_{ch,in}=4$. As expected, no exergy can be recovered when $\overline{T}_{ch,in}\le\overline{T}_m$ ($\overline{T}_{d,in}\ge\overline{T}_m$) since no energy can be stored (or extracted). An optimal value of $\overline{T}_m$ exists for any $\overline{T}_{d,in}$ and $\overline{T}_{ch,in}$ corresponding to a maximum amount of exergy recovered. Importantly, the dependence of the exergy efficiency on $\overline{T}_m$ has no quantitative or qualitative resemblance to the χ dependence. As evident in Fig. 19, the melting temperatures associated with maximum exergy efficiency, ε, correspond to exergy recovery of zero. This is consistent with exergy analyses for similar energy generation systems that reveal that high second-law efficiencies often correspond to vanishingly small power output [76,77].

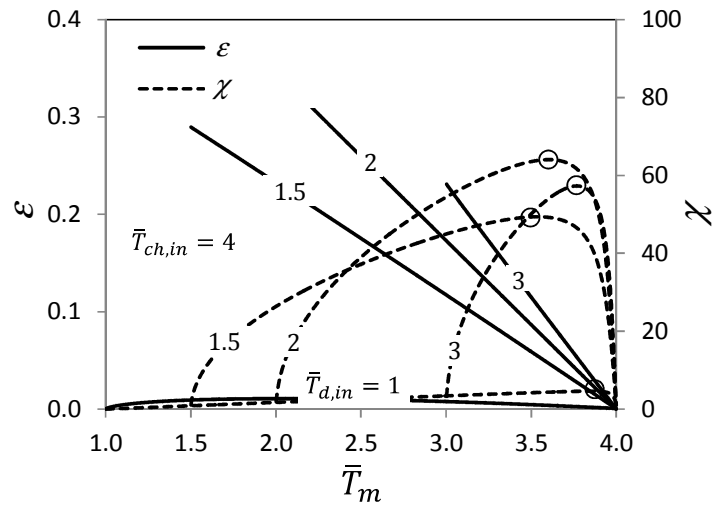

Fig. 19. Variations of the exergy efficiency and dimensionless exergy recovery with dimensionless melting temperature for dimensionless charging temperature of $\bar{T}_{ch,in}$ = 4 and various discharging inlet temperatures. Optimal exergy recovery conditions are shown by the open circles.

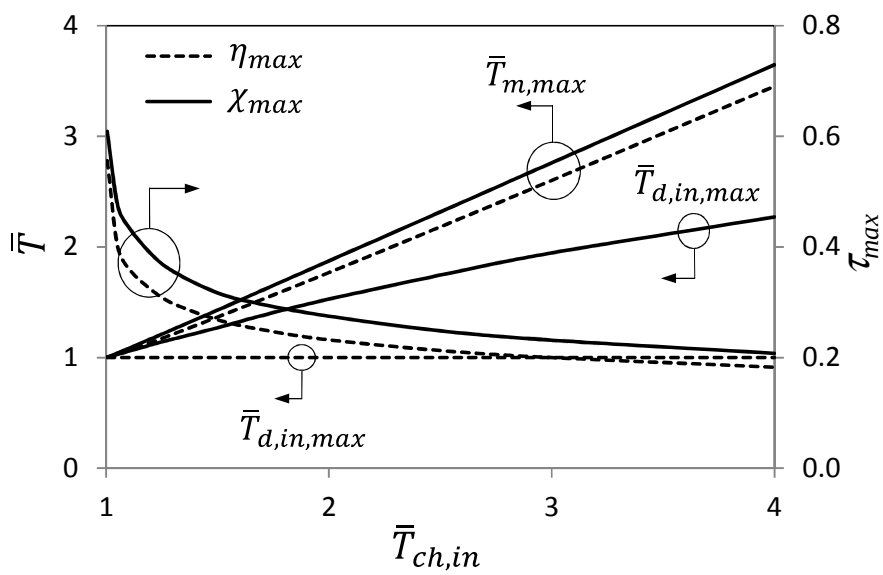

Fig. 20. The base case (A_r = 1) $\bar{T}_m$ and $\bar{T}_{d,in}$ and τ that yield the maximum energy storage and exergy recovery.

For any specified value of $\bar{T}_{ch,in}$, it has been shown that specific values of $\bar{T}_{d,in}$, $\bar{T}_m$ and τ are required to maximize either the energy stored (η), or the exergy recovered (χ). These predictions are generalized in Fig. 20. The phase change temperature required to maximize either the energy stored or the exergy recovered, $\bar{T}_{m,max}$, increases as $\bar{T}_{ch,in}$ increases, as discussed previously. Similarly, the required HTF inlet temperature during discharging, $\bar{T}_{d,in,max}$, increases if χ is to be maximized, and achieves a value of unity if η is maximized. The dimensionless charging time, τ_{max}, decreases as $\bar{T}_{ch,in}$ increases, as expected. Because of the dependence of the extracted exergy on the HTF outlet

temperature, the required phase change temperature to maximize χ always exceeds the value of $\overline{T}_m$ necessary to maximize η. Also, because the temperature difference between the HTF (during charging) and the PCM needed to maximize χ is smaller than the corresponding temperature difference required to maximize η, the charging time to maximize the exergy extracted from the storage system exceeds the charging time required to maximize the energy storage for any value of $\overline{T}_{ch,in}$.

The influence of adding extended surfaces on the PCM side (Fig. 18c) on the χ_{max} of the LHTES is illustrated in Fig. 21. Increasing the surface area of the PCM side by a factor of 10 results in a six-fold increase in the exergy extracted from the LHTES system. This improvement is considered to be significant, and is due mainly to the increased heat transfer rates and, in turn, increased HTF temperature during discharging.

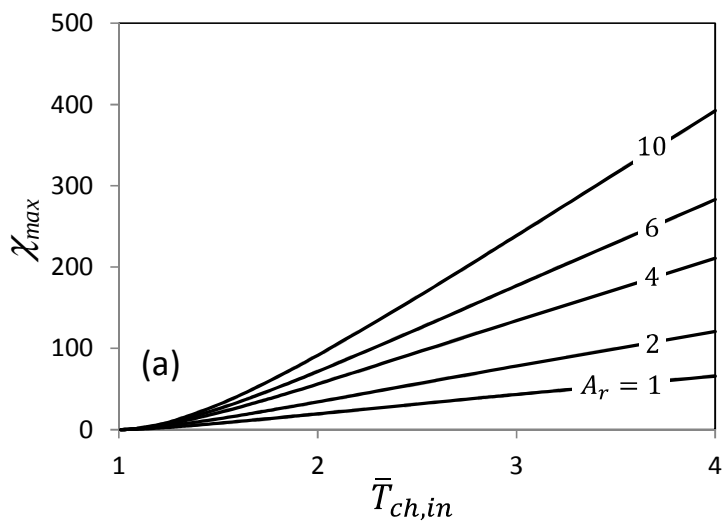

Fig. 21. Effect of adding extended surfaces on (a) χ_{max} for given $\overline{T}_{ch,in}$.

Detailed Numerical Modeling:

Wang et al. [78] developed a comprehensive and efficient numerical model for melting with natural convection is developed. The model is based on the finite volume approach and temperature transforming model. A new method for solid velocity correction with an explicit update for melting front and buoyancy force (the governing equations are otherwise discretized in fully implicit format) is proposed and shown to be very effective in eliminating inconsistencies found in previous studies. The predictions of the proposed numerical model are compared to previous theoretical, modeling and experimental results, and reasonable agreement is achieved. It is shown that the consistent update technique (CUT) algorithm is much more efficient (CPU time reduce by an order of magnitude) than the SIMPLE algorithm for solving melting problems. Furthermore, it is demonstrated that the central difference scheme is much more accurate than the power law scheme, and that the Richardson extrapolation method provides a powerful tool for grid and time step independence tests as well as discretization error estimates. Finally, it is found that melting phenomena of octadecane

and sodium nitrate, both melting in a square cavity with a Rayleigh number of 10^8 and a Stefan number of 0.1, are essentially identical; such a similarity can be used as a foundation for conducting room temperature experiments to investigate the melting/solidification characteristics of high temperature phase change materials (PCMs). A benchmark solution for the entire melting process of sodium nitrate is provided as well.

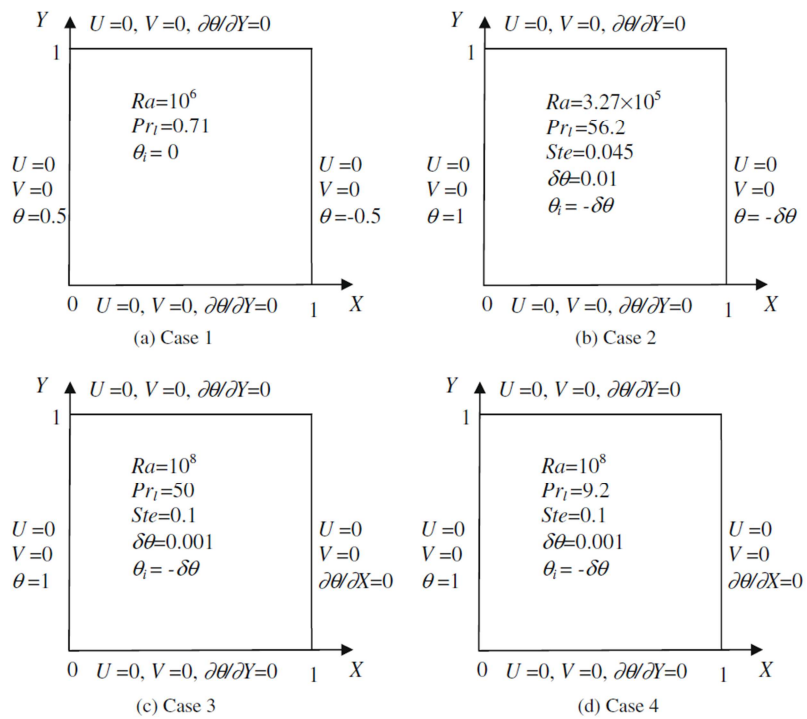

Fig. 22. Problem definition for Cases 1–4.

Four cases, as shown in Fig. 22, are selected to demonstrate the proposed methods. Although the geometric configurations of all the cases are the same, there are particular reasons for examining each case. The first case is the classical problem of natural convection of air in a square cavity, and there is no melting involved. The second case is the problem of octadecane melting with natural convection in a square cavity. In the last two cases, as shown in Fig. 22, melting of octadecane and that of sodium nitrate ($NaNO_3$), both at a Rayleigh number of 10^8 and a Stefan number of 0.1, are modeled.

The results of Cases 3 and 4 are compared in Fig. 23, together with (i) the conduction solution as well as (ii) the correlations by Jany and Bejan [79]. Although a small difference can be seen between Cases 3 and 4 in terms of the melting front (Fig. 23a) and Nusselt number (Fig. 23b) results, it is negligibly small for any engineering application. Therefore, an experimental study involving Case 3 would be sufficient for understanding the melting process of Case 4. It is clear from Fig. 23 that the natural convection in the liquid phase substantially enhances heat transfer, when the modeling results with natural convection are compared with those considering conduction only. The predictions of the correlations developed by Jany and Bejan [79] agree very well

with the present model in terms of the accumulated heat inputs, which are of most concern in thermal energy storage applications, but the agreement in the Nusselt number and liquid fraction results is just fair. It should be noted that there are no correlations to compare with for the stage after the melting front reaches the right wall at around SteFo = 0.014.

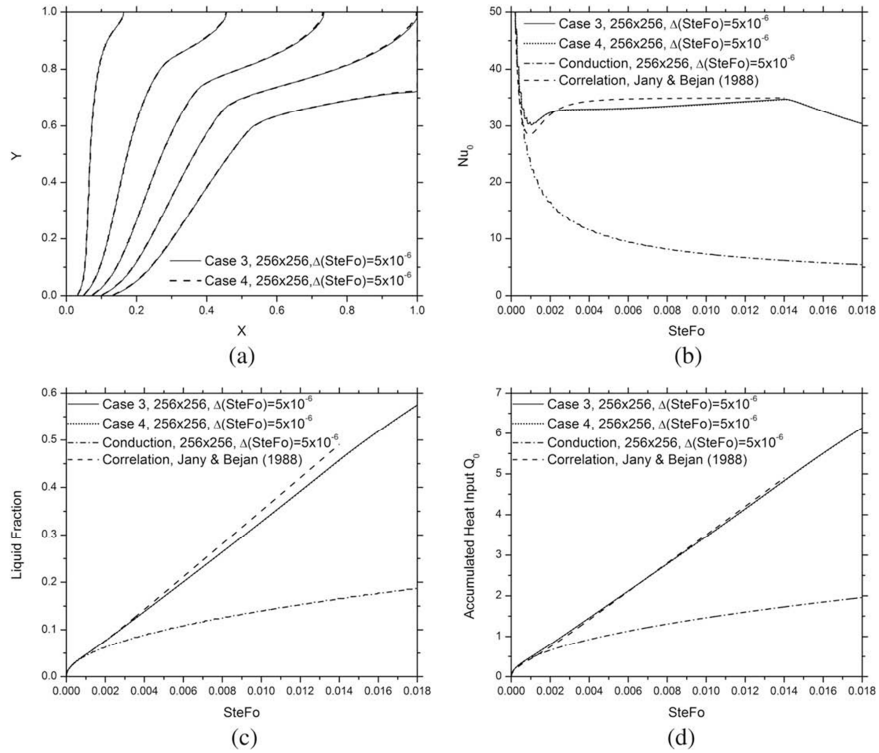

Fig. 23. Results for Cases 3 and 4: (a) the melting front locations at SteFo = 0.002, 0.006, 0.01, 0.014, and 0.018, respectively, and the temporal evolution of (b) the Nusselt number, (c) the liquid fraction, and (d) the accumulated heat input. The results of the conduction-only solution and the predictions using correlations proposed by Jany and Bejan [79] **are compared as well.**

Sharifi et al. [80] developed a comprehensive numerical model to simulate the heat pipe-assisted melting of a phase change material (PCM) housed within a vertical cylindrical enclosure. The results were compared to melting induced by heating from an isothermal surface, or with a solid rod or a hollow tube. A parametric study reveals that the heat pipe-assisted melting rates are significantly higher than those associated with the rod or tube, and approach the maximum attainable rates associated with the isothermal surface. Melting rates are enhanced as either the condenser length or the diameter of the heat pipe is increased. The heat pipe is particularly effective in augmenting melting in configurations involving PCM heating from above.

The computational domain and geometric dimensions associated with the heat pipe-PCM system are shown in Fig. 24. The vertically-oriented heat pipe is subdivided into three radial regions: the working fluid vapor, the porous wick that is imbibed with the liquid working fluid, and the solid wall. The PCM is contained in the vertical cylindrical annulus of length L_c, which surrounds the condenser section of the heat pipe which is also of length L_c. The adiabatic transport section of the heat pipe (of length L_a) and the heat pipe's evaporator section (of length L_e) form the lower portion of the system. The

isothermal surface, rod and tube each have the same exterior dimensions as the heat pipe. The tube has a wall thickness of 1 mm and is evacuated. Heating from below (HFB) and from above (HFA) are both considered, and the direction of heating is specified by switching the orientation of the gravitational acceleration vector.

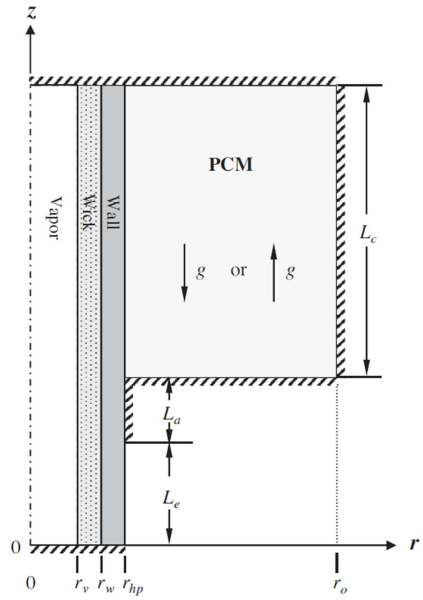

Fig. 24. Physical model and computational domain for the heat pipe and PCM.

The detailed numerical methodology used here is described in Wang et al. [78,81] and is summarized as follows. The standard finite volume method of Patankar [82] is used to discretize the descriptive equations, and the central differencing scheme is applied to the advection and diffusion terms. A fully-implicit scheme is used for the time discretization, employing a standard underrelaxation version of the consistent update technique [83] or SUV-CUT. An explicit update scheme is utilized to evaluate the buoyancy source term in the momentum equation. A pressure-decoupled solid velocity correction is used to enforce zero velocity in the solid PCM as well as in the heat pipe wall and wick. A V-cycle based multigrid solver [84] with the SIP [85] smoother is employed to solve the algebraic equations accurately and efficiently.

Fig. 25 shows temperature distributions within the tall, L_e = 70 mm module equipped with the D_{hp} = 14 mm heat pipe (top), and rod (bottom) at various times associated with similar melt fractions for the three cases. A melt fraction of $f_l \approx 0.67$ is achieved at $t \approx 3$ and 7 for the heat pipe, rod, respectively. Since the thermal resistance posed by the heat pipe is small (as is its thermal capacitance) relatively uniform temperatures exist along the length of its condensing section, inducing the highest melting rates. Temperature distributions within the working fluid of the heat pipe bear similarity to those reported elsewhere [51] and are influenced by vapor velocities as high as ≈ 100 m/s. As expected, melting along the heat pipe is nearly uniform at early times (t = 0.5 h), since heat transfer within the molten PCM is conduction-dominated. As the melt region expands and natural convection becomes established, melting rates become more pronounced near the top of the enclosure, as warm molten PCM is brought into proximity with the PCM solid–liquid interface by way of the overall clockwise circulation in the melt.

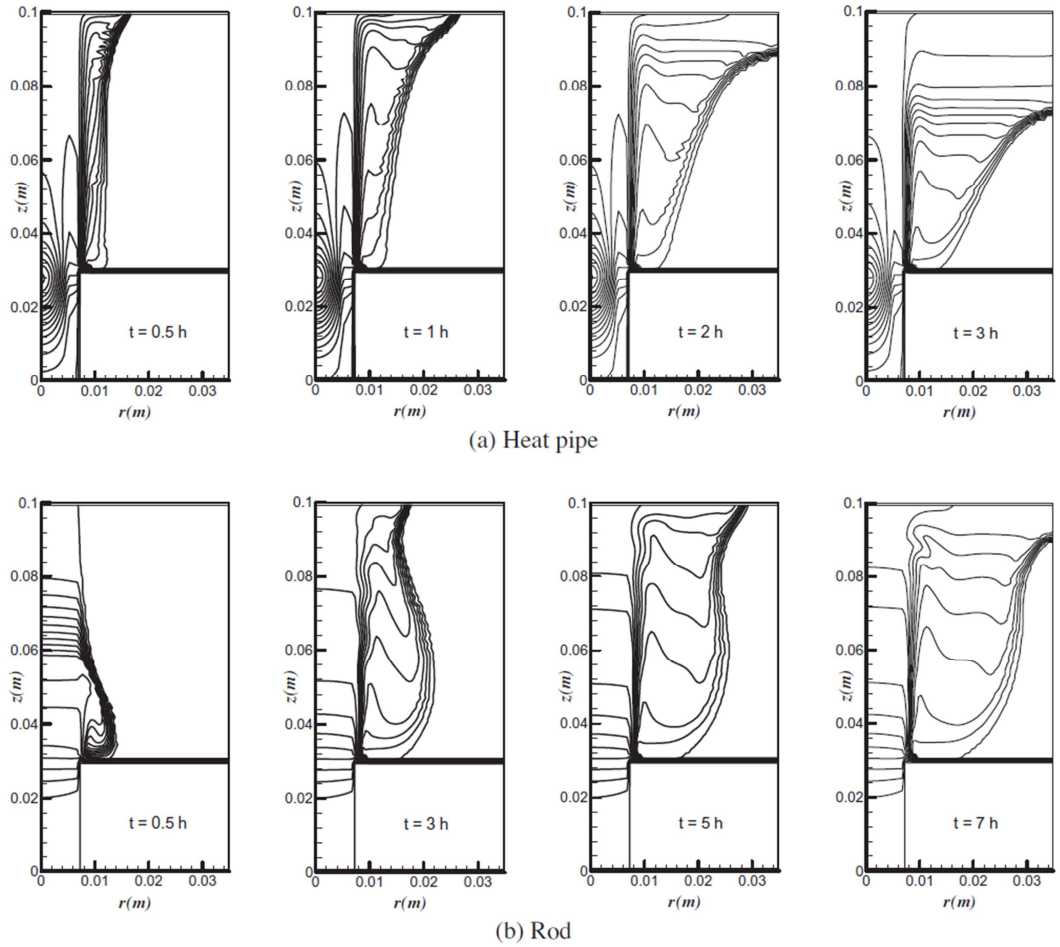

Fig. 25. Temperature distributions for the tall module (L_c = 70 mm): (a) heat pipe, and (b) rod. Isotherms are shown at intervals of 0.2 K (1 K) over the range 580 K < T < 582 K for the rod case. Isotherms are shown at intervals of 0.5 K for 580 K < T < 591 K for the heat pipe case.

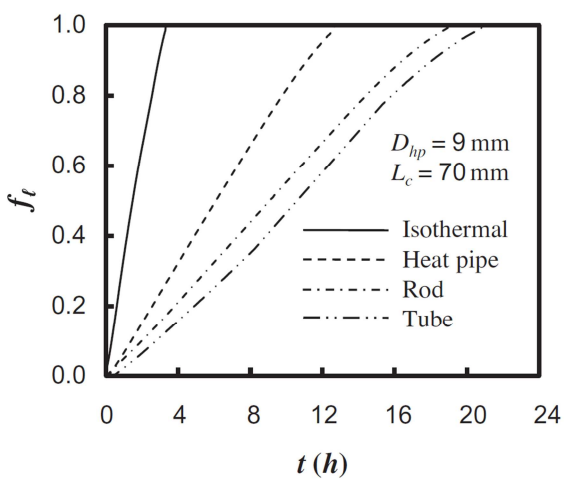

Fig. 26. Liquid fraction histories.

Use of the solid rod (Fig. 25b) induces intermediate melting rates, where warm temperatures have not yet propagated extensively to the upper sections of the rod for *t*

= 0.5 h. The melt region topographies are similar to those of the heat pipe at later times (t = 7 h) during which the rod is more uniformly-warm. The predictions are in qualitative agreement with experimental measurements of heat pipe- and rod-assisted PCM melting [60]. The temporal variations of the liquid PCM fraction are shown in Fig. 26. The melting rate associated with heat pipe is almost two times that of tube, while melting rates of tube and rod are not substantially different. Almost linear profiles are observed for all cases which stresses the natural-convection controlled heat transfer rates during melting.

Wang et al. [86] employed the finite-volume model developed in [78] to analyze alternate melting and solidification, which is the fundamental operational mode of latent thermal energy storage (LTES) systems. The simulated cases include: (1) melting of tin with natural convection, (2) alternate melting and solidification of sodium nitrate, and (3) cyclic phase change of gallium. For each case, temporal evolution of the heat transfer rate and liquid fraction is presented. In addition, snapshots of phase interface, temperature, pressure, and liquid velocity distributions are presented. The implications of the modeling results are discussed.

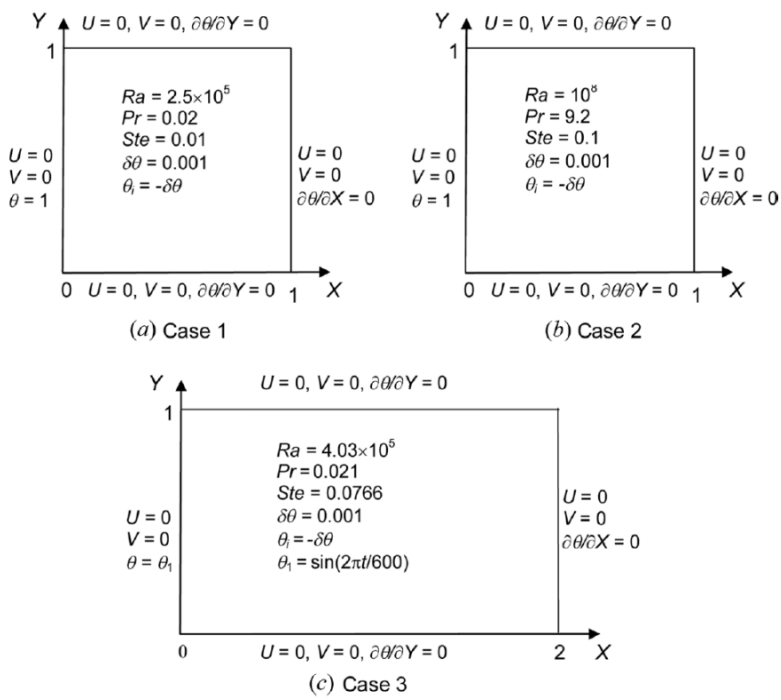

Fig. 27. Problem definitions for Cases 1–3.

Three cases, shown in Fig. 27, are considered. The first case is a benchmark problem for melting with natural convection of low-Prandtl-number PCMs. The primary reason for selecting this case is that it has been extensively studied in the literature [87–89] and thus provides a quantitative comparison for our numerical methods. The second case involves sodium nitrate subject to alternate melting and solidification controlled by a stepwise-varying boundary temperature. The solid–liquid phase change of sodium nitrate has rarely been investigated in the literature. However, this material is a promising PCM for LTES systems proposed. The last case pertains to gallium that is

subjected to a sinusoidal wall temperature variation and, in turn, cyclic phase change. This case was originally studied by Voller et al. [90].

Fig. 28 shows the prescribed boundary temperature, and the temporal evolution of the heat input rate, the liquid fraction, and the accumulated heat input for 13 phase-change cycles for Case 3. Fig. 28c and Fig. 28d suggest that the response can be divided into two stages, similar to the two regimes (the initial transient oscillatory regime and the steady periodical melting regime) reported in [91] and [92]. In the first stage, consisting of the first 10 cycles, both the liquid fraction and the accumulated heat input increase with time, in addition to the regular oscillation within a single cycle. In the second stage, the liquid fraction and accumulated heat input vary within a single cycle, while negligible difference exists between cycles, indicating a quasi-steady behavior. Both the asymmetric nature of each cycle and the increases in liquid fraction and accumulated heat input during the first stage are attributed to the effects of natural convection. The transition from the first stage to the second, quasi-steady stage is also marked by the liquid fraction reaching unity. In the second stage, once the solid phase disappears, the temperature of the entire system can exceed the melting point, which retards further heat input and favors the subsequent heat extraction. This mechanism provides a basis for establishing the quasi-steady state.

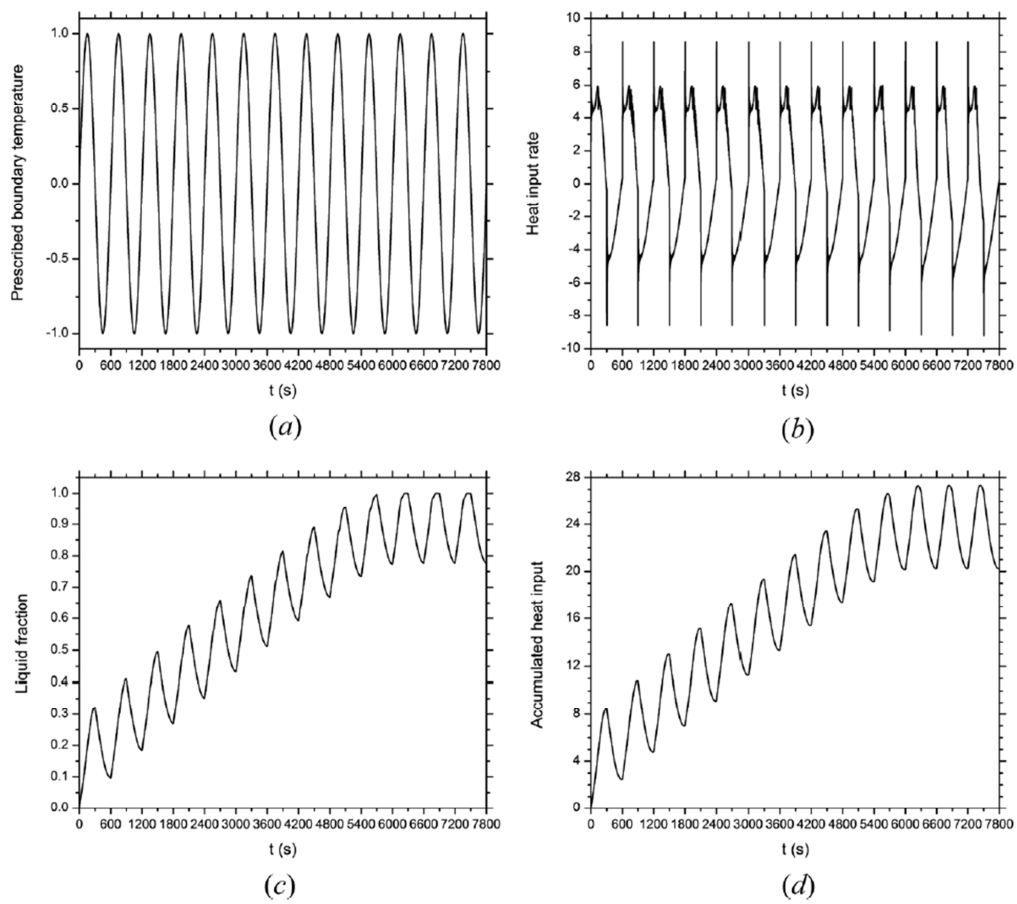

Fig. 28. Results for Cyclic Phase Change of Gallium (Case 3): (a) the prescribed boundary temperature, and the temporal evolution of (b) the heat input rate, (c) the liquid fraction, and (d) the accumulated heat input.

The phase interface evolution for the entire process is depicted in Fig. 29, with Fig. 29a showing the melting fronts at the midpoint of each cycle, when the prescribed boundary temperature drops from superheating to the melting point, and Fig. 29b showing phase interfaces at the end of each cycle, when the boundary temperature increases from subcooling to the melting point. Fig. 29c and Fig. 29d show the phase interface progressing during the 6th cycle, while Fig. 29e and Fig. 29f show it for the 13th cycle. The phase interfaces shown in Fig. 29 are significantly different from those reported by Voller et al. [90] for the same problem.

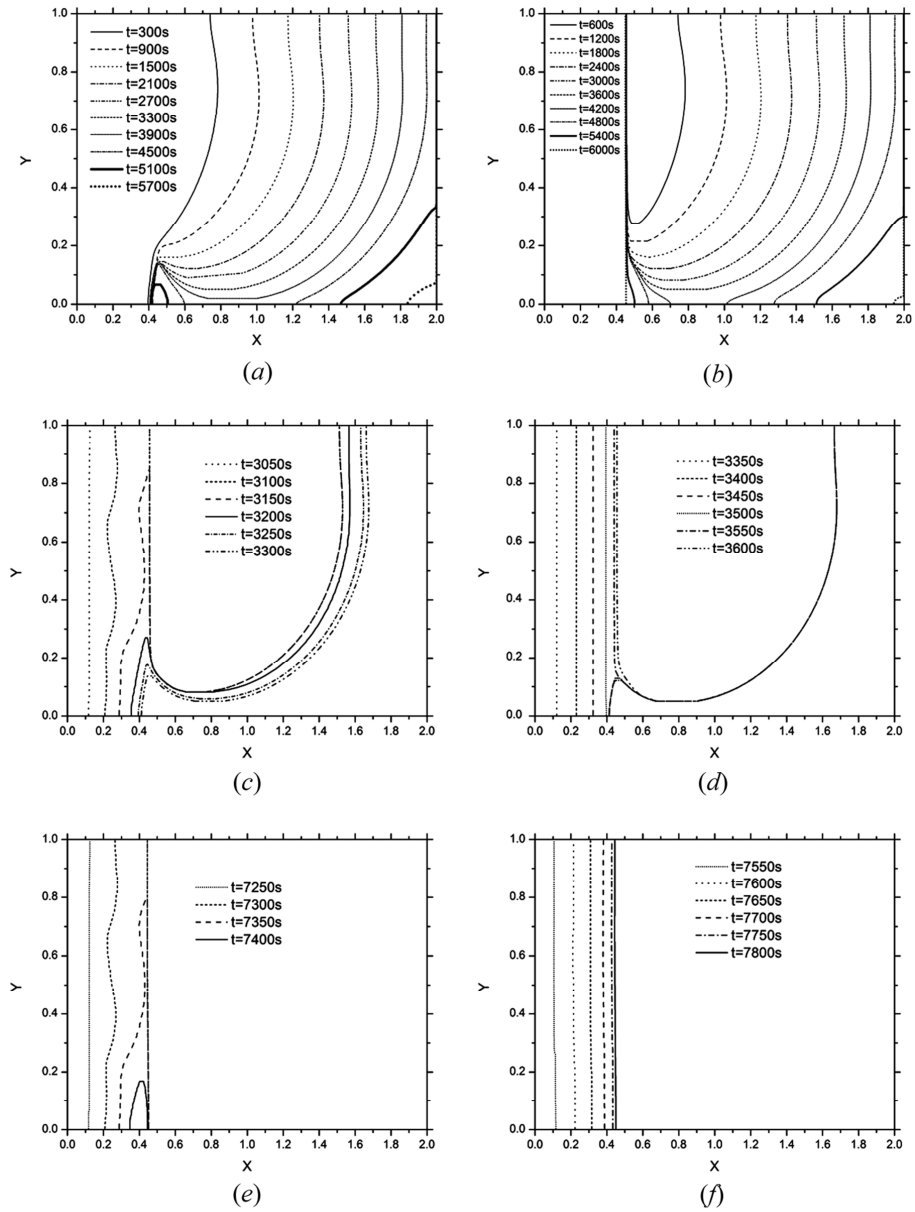

Fig. 29. Results for Case 3: phase interfaces at various times.

Within the limit of the numerical errors, including the simplifying assumptions, the following conclusions are drawn.

1. Sufficiently accurate numerical schemes and sufficiently fine grids are required to capture the detailed boundary-layer structure, multicellular convection, and intrinsic oscillation associated with natural convection in the molten PCM.

2. The high-frequency oscillation during melting of low-Prandtl-number PCMs contributes little to the liquid fraction and accumulated heat input evolution, and can be filtered out by adopting larger time steps in an engineering analysis. Such a strategy can substantially reduce the computational expense of the simulation.

3. The natural convection in the liquid phase enhances heat transfer during melting. In a LHTES system for concentrating solar power applications, for example, either (a) a longer discharging period relative to the charging period, (b) a greater degree of subcooling relative to superheating, or (c) additional heat transfer enhancement techniques are required to balance the system's thermal response.

4. As for previously reported results involving high-Prandtl-number PCMs, the effects of natural convection make a low-Pr LHTES system that is subjected to cyclic heating and cooling prone to two stages of operation. The initial stage precedes the quasi-steady stage, and can be quite long. Care must be taken when extrapolating predictions that may cover only a few charging and discharging cycles to quasi-steady behavior.

Conclusions:

The extensive experimental, system level and detailed numerical simulation efforts carried out during the course of this project demonstrate the superior performance of heat pipes/thermosyphons for integration with latent heat thermal energy storage systems to enhance the heat transfer rates and reduce the overall thermal resistances, thereby decreasing the levelized cost of solar electricity generation. Economic evaluation of such heat pipe/thermosyphon integrated latent heat thermal energy storage systems showed that these systems are cost-competitive with the state of the art thermal energy storage technologies currently in use. Efficient system level modeling tools, leveraged by the input from detailed comprehensive numerical simulations, were developed to aid the process of design and optimization of large-scale hybrid HP-PCM thermal energy storage systems. The candidate materials for the PCM, heat pipe shell and heat pipe working fluid were identified considering compatibility and cost issues. Besides the heat transfer analysis, an exergy analysis was also carried out to investigate the performance of HP/TS-assisted LHTES systems in view of the potential to produce useful work, and new measures were proposed for the exergy analysis of LHTES systems employed in solar applications. Overall, all the performed experimental and theoretical investigations consistently demonstrated the potential of HP/TS-assisted LHTES systems to meet the required heat transfer performance and exergy efficiencies while being cost-competitive.

Path Forward:

Further improvement of the LHTES systems can be achieved by identifying cost-effective PCMs characterized by chemical stability, high energy density and compatibility with the HP shell materials. Manufacturing techniques need to be developed for mass production of HPs/TSs and to assemble the large scale HP/TS-

assisted LHTES units in an efficient manner. Combination of HP/TS-assisted LHTES systems with other heat transfer enhancement techniques has the potential to significantly reduce the overall thermal resistance within the storage system, thereby reducing the cost. Also, integration of LHTES systems with other thermal energy storage technologies, including sensible thermal energy storage based systems, can be beneficial in some solar applications.

References:

[1] S. Kakac, E. Paykoc, and Y. Yender, "Storage of Solar Thermal Energy," In *Energy Storage Systems* (eds B. Kilkisş & S. Kakaç), Springer, Netherlands, Dordrecht, 1989.

[2] I. Dincer, and M.A. Rosen, *Thermal Energy Storage: Systems and Applications*, Wiley, 2002.

[3] U. Herrmann, and D.W. Kearney, "Survey of thermal energy storage for parabolic trough power plants," *Journal of Solar Energy Engineering*, Vol. 124, No. 2, pp. 145, 2002. http://dx.doi.org/10.1115/1.1467601

[4] J.E. Pacheco, S.K. Showalter, and W.J. Kolb, "Development of a molten-salt thermocline thermal storage system for parabolic trough plants," *Journal of Solar Energy Engineering*, Vol. 124, No. 2, pp. 153, 2002. http://dx.doi.org/10.1115/1.1464123

[5] H. Price, E. Lüpfert, D. Kearney, E. Zarza, G. Cohen, R. Gee, and R. Mahoney, "Advances in parabolic trough solar power technology," *Journal of Solar Energy Engineering*, Vol. 124, No. 2, pp. 109, 2002. http://dx.doi.org/10.1115/1.1467922

[6] Z.A. Hammou, and M. Lacroix, "A new PCM storage system for managing simultaneously solar and electric energy," *Energy and Buildings*, Vol. 38, No. 3, pp. 258–265, 2006. http://dx.doi.org/10.1016/j.enbuild.2005.06.008

[7] M. Kenisarin, and K. Mahkamov, "Solar energy storage using phase change materials," *Renewable and Sustainable Energy Reviews*, Vol. 11, No. 9, pp. 1913–1965, 2007. http://dx.doi.org/10.1016/j.rser.2006.05.005

[8] R. Tamme, T. Bauer, J. Buschle, D. Laing, H. Müller-Steinhagen, and W.-D. Steinmann, "Latent heat storage above 120°C for applications in the industrial process heat sector and solar power generation," *International Journal of Energy Research*, Vol. 32, No. 3, pp. 264–271, 2008. http://dx.doi.org/10.1002/er.1346

[9] W.-D. Steinmann, and R. Tamme, "Latent heat storage for solar steam systems," *Journal of Solar Energy Engineering*, Vol. 130, No. 1, pp. 011004, 2008. http://dx.doi.org/10.1115/1.2804624

[10] P. Verma, and S. Singal, "Review of mathematical modeling on latent heat thermal energy storage systems using phase-change material," *Renewable and Sustainable Energy Reviews*, Vol. 12, No. 4, pp. 999–1031, 2008. http://dx.doi.org/10.1016/j.rser.2006.11.002

[11] J. Stekli, "Technical challenges and opportunities for concentrating solar power with thermal energy storage," *Journal of Thermal Science and Engineering Applications*, Vol. 5, No. 2, pp. 021011, 2013. http://dx.doi.org/10.1115/1.4024143

[12] Q. He, and W. Zhang, "A study on latent heat storage exchangers with the high-temperature phase-change material," *International Journal of Energy Research*, Vol. 25, No. 4, pp. 331–341, 2001. http://dx.doi.org/10.1002/er.683

[13] H. Cui, X. Yuan, and X. Hou, "Thermal performance analysis for a heat receiver using multiple phase change materials," *Applied Thermal Engineering*, Vol. 23, No. 18, pp. 2353–2361, 2003. http://dx.doi.org/10.1016/S1359-4311(03)00210-2

[14] R. Tamme, D. Laing, and W.-D. Steinmann, "Advanced thermal energy storage technology for parabolic trough," *Journal of Solar Energy Engineering*, Vol. 126, No. 2, pp. 794, 2004. http://dx.doi.org/10.1115/1.1687404

[15] H. Michels, and R. Pitz-Paal, "Cascaded latent heat storage for parabolic trough solar power plants," *Solar Energy*, Vol. 81, No. 6, pp. 829–837, 2007. http://dx.doi.org/10.1016/j.solener.2006.09.008

[16] H. Cui, Y. Xing, Y. Guo, Z. Wang, H. Cui, and X. Yuan, "Numerical simulation and experiment investigation on unit heat exchange tube for solar heat receiver," *Solar Energy*, Vol. 82, No. 12, pp. 1229–1234, 2008. http://dx.doi.org/10.1016/j.solener.2008.06.009

[17] Krishnan, S, Murthy, JY, Garimella, and SV, "A two-temperature model for solid-liquid phase change in metal foams," Vol. 127, No. 9, pp. 995–1004, 2005. http://dx.doi.org/10.1115/1.201494

[18] S.-T. Hong, and D.R. Herling, "Open-cell aluminum foams filled with phase change materials as compact heat sinks," *Scripta Materialia*, Vol. 55, No. 10, pp. 887–890, 2006. http://dx.doi.org/10.1016/j.scriptamat.2006.07.050

[19] V. Morisson, M. Rady, E. Palomo, and E. Arquis, "Thermal energy storage systems for electricity production using solar energy direct steam generation technology," *Chemical Engineering and Processing: Process Intensification*, Vol. 47, No. 3, pp. 499–507, 2008. http://dx.doi.org/10.1016/j.cep.2007.01.025

[20] A. Siahpush, J. O'Brien, and J. Crepeau, "Phase change heat transfer enhancement using copper porous foam," *Journal of Heat Transfer*, Vol. 130, No. 8, pp. 082301, 2008. http://dx.doi.org/10.1115/1.2928010

[21] J. Fukai, M. Kanou, Y. Kodama, and O. Miyatake, "Thermal conductivity enhancement of energy storage media using carbon fibers," *Energy Conversion and Management*, Vol. 41, No. 14, pp. 1543–1556, 2000. http://dx.doi.org/10.1016/S0196-8904(99)00166-1

[22] J. Fukai, Y. Hamada, Y. Morozumi, and O. Miyatake, "Effect of carbon-fiber brushes on conductive heat transfer in phase change materials," *International Journal of Heat and Mass Transfer*, Vol. 45, No. 24, pp. 4781–4792, 2002. http://dx.doi.org/10.1016/S0017-9310(02)00179-5

[23] Y. Zhang, and A. Faghri, "Heat transfer enhancement in latent heat thermal energy storage system by using the internally finned tube," *International Journal of Heat and Mass Transfer*, Vol. 39, No. 15, pp. 3165–3173, 1996. http://dx.doi.org/10.1016/0017-9310(95)00402-5

[24] A. Erek, Z. Ilken, and M.A. Acar, "Experimental and numerical investigation of thermal energy storage with a finned tube," *International Journal of Energy Research*, Vol. 29, No. 4, pp. 283–301, 2005. http://dx.doi.org/10.1002/er.1057

[25] V. Shatikian, G. Ziskind, and R. Letan, "Numerical investigation of a PCM-based heat sink with internal fins: Constant heat flux," *International Journal of Heat and Mass Transfer*, Vol. 51, No. 5–6, pp. 1488–1493, 2008. http://dx.doi.org/10.1016/j.ijheatmasstransfer.2007.11.036

[26] K. Ermis, A. Erek, and I. Dincer, "Heat transfer analysis of phase change process in a finned-tube thermal energy storage system using artificial neural network," *International Journal of Heat and Mass Transfer*, Vol. 50, No. 15–16, pp. 3163–3175, 2007. http://dx.doi.org/10.1016/j.ijheatmasstransfer.2006.12.017

[27] C. Guo, and W. Zhang, "Numerical simulation and parametric study on new type of high temperature latent heat thermal energy storage system," *Energy Conversion and Management*, Vol. 49, No. 5, pp. 919–927, 2008. http://dx.doi.org/10.1016/j.enconman.2007.10.025

[28] M. Gharebaghi, and I. Sezai, "Enhancement of heat transfer in latent heat storage modules with internal fins," *Numerical Heat Transfer, Part A: Applications*, Vol. 53, No. 7, pp. 749–765, 2007. http://dx.doi.org/10.1080/10407780701715786

[29] R.V. Seeniraj, and N. Lakshmi Narasimhan, "Performance enhancement of a solar dynamic LHTS module having both fins and multiple PCMs," *Solar Energy*, Vol. 82, No. 6, pp. 535–542, 2008. http://dx.doi.org/10.1016/j.solener.2007.11.001

[30] K. Kaygusuz, "Experimental and theoretical investigation of latent heat storage for water based solar heating systems," *Energy Conversion and Management*, Vol. 36, No. 5, pp. 315–323, 1995. http://dx.doi.org/10.1016/0196-8904(95)98896-U

[31] M. Akgün, O. Aydın, and K. Kaygusuz, "Thermal energy storage performance of paraffin in a novel tube-in-shell system," *Applied Thermal Engineering*, Vol. 28, No. 5–6, pp. 405–413, 2008. http://dx.doi.org/10.1016/j.applthermaleng.2007.05.013

[32] S. Kalaiselvam, M. Veerappan, A. Arul Aaron, and S. Iniyan, "Experimental and analytical investigation of solidification and melting characteristics of PCMs inside cylindrical encapsulation," *International Journal of Thermal Sciences*, Vol. 47, No. 7, pp. 858–874, 2008. http://dx.doi.org/10.1016/j.ijthermalsci.2007.07.003

[33] A. Erek, and I. Dincer, "Numerical heat transfer analysis of encapsulated ice thermal energy storage system with variable heat transfer coefficient in downstream," *International Journal of Heat and Mass Transfer*, Vol. 52, No. 3–4, pp. 851–859, 2009. http://dx.doi.org/10.1016/j.ijheatmasstransfer.2008.06.024

[34] S.M. Aceves, H. Nakamura, G.M. Reistad, and J. Martinez-Frias, "Optimization of a class of latent thermal energy storage systems with multiple phase-change

materials," *Journal of Solar Energy Engineering*, Vol. 120, No. 1, pp. 14, 1998. http://dx.doi.org/10.1115/1.2888040

[35] Z.-X. Gong, and A.S. Mujumdar, "Enhancement of energy charge-discharge rates in composite slabs of different phase change materials," *International Journal of Heat and Mass Transfer*, Vol. 39, No. 4, pp. 725–733, 1996. http://dx.doi.org/10.1016/0017-9310(95)00179-4

[36] Z.-X. Gong, and A.S. Mujumdar, "Thermodynamic optimization of the thermal process in energy storage using multiple phase change materials," *Applied Thermal Engineering*, Vol. 17, No. 11, pp. 1067–1083, 1997. http://dx.doi.org/10.1016/S1359-4311(97)00012-4

[37] T. Watanabe, and A. Kanzawa, "Second law optimization of a latent heat storage system with PCMS having different melting points," *Heat Recovery Systems and CHP*, Vol. 15, No. 7, pp. 641–653, 1995. http://dx.doi.org/10.1016/0890-4332(95)90044-6

[38] A. Faghri, "Thermal energy storage heat exchanger," 1990.

[39] A. Faghri, "Thermal energy storage system," 1991.

[40] A. Faghri, *Heat Pipe Science and Technology*, Taylor & Francis Group, Washington, DC, 1995.

[41] Z. Liu, Z. Wang, and C. Ma, "An experimental study on heat transfer characteristics of heat pipe heat exchanger with latent heat storage. Part I: Charging only and discharging only modes," *Energy Conversion and Management*, Vol. 47, No. 7–8, pp. 944–966, 2006. http://dx.doi.org/10.1016/j.enconman.2005.06.004

[42] B. Horbaniuc, G. Dumitrascu, and A. Popescu, "Mathematical models for the study of solidification within a longitudinally finned heat pipe latent heat thermal storage system," *Energy Conversion and Management*, Vol. 40, No. 15–16, pp. 1765–1774, 1999. http://dx.doi.org/10.1016/S0196-8904(99)00069-2

[43] F. Tardy, and S.M. Sami, "Thermal analysis of heat pipes during thermal storage," *Applied Thermal Engineering*, Vol. 29, No. 2–3, pp. 329–333, 2009. http://dx.doi.org/10.1016/j.applthermaleng.2008.02.037

[44] D. Etheridge, K. Murphy, and D. Reay, "A PCM/heat pipe cooling system for reducing air conditioning in buildings: review of options and report on field tests," *Building Services Engineering Research and Technology*, Vol. 27, No. 1, pp. 27–39, 2006. http://dx.doi.org/10.1191/0143624406bt142oa

[45] W.-S. Lee, B.-R. Chen, and S.-L. Chen, "Latent heat storage in a two-phase thermosyphon solar water heater," *Journal of Solar Energy Engineering*, Vol. 128, No. 1, pp. 69, 2006. http://dx.doi.org/10.1115/1.2147588

[46] M. Aghvami, and A. Faghri, "Analysis of flat heat pipes with various heating and cooling configurations," *Applied Thermal Engineering*, Vol. 31, No. 14–15, pp. 2645–2655, 2011. http://dx.doi.org/10.1016/j.applthermaleng.2011.04.034

[47] H. Shabgard, and A. Faghri, "Performance characteristics of cylindrical heat pipes with multiple heat sources," *Applied Thermal Engineering*, Vol. 31, No. 16, pp. 3410–3419, 2011. http://dx.doi.org/10.1016/j.applthermaleng.2011.06.026

[48] T. Kaya, and J. Goldak, "Three-dimensional numerical analysis of heat and mass transfer in heat pipes," *Heat and Mass Transfer*, Vol. 43, No. 8, pp. 775–785, 2006. http://dx.doi.org/10.1007/s00231-006-0166-y

[49] J.-M. Tournier, and M.S. El-Genk, "A heat pipe transient analysis model," *International Journal of Heat and Mass Transfer*, Vol. 37, No. 5, pp. 753–762, 1994. http://dx.doi.org/10.1016/0017-9310(94)90113-9

[50] J.-M. Tournier, and M.S. El-Genk, "Segregated solution technique for simulating the transient operation of heat pipes," *Numerical Heat Transfer, Part B: Fundamentals*, Vol. 25, No. 3, pp. 331–355, 1994. http://dx.doi.org/10.1080/10407799408955924

[51] Y. Cao, and A. Faghri, "Transient two-dimensional compressible analysis for high-temperature heat pipes with pulsed heat input," *Numerical Heat Transfer, Part A: Applications*, Vol. 18, No. 4, pp. 483–502, 1991. http://dx.doi.org/10.1080/10407789008944804

[52] J.A. Rice, and A. Faghri, "Analysis of screen wick heat pipes, including capillary dry-out limitations," *Journal of Thermophysics and Heat Transfer*, Vol. 21, No. 3, pp. 475–486, 2007. http://dx.doi.org/10.2514/1.24809

[53] C.-J. Ho, and R. Viskanta, "Heat transfer during melting from an isothermal vertical wall," *Journal of Heat Transfer*, Vol. 106, No. 1, pp. 12, 1984. http://dx.doi.org/10.1115/1.3246624

[54] B.W. Webb, and R. Viskanta, "Natural-convection-dominated melting heat transfer in an inclined rectangular enclosure," *International Journal of Heat and Mass Transfer*, Vol. 29, No. 2, pp. 183–192, 1986. http://dx.doi.org/10.1016/0017-9310(86)90226-7

[55] T.L. Bergman, and B.W. Webb, "Simulation of pure metal melting with buoyancy and surface tension forces in the liquid phase," *International Journal of Heat and Mass Transfer*, Vol. 33, No. 1, pp. 139–149, 1990. http://dx.doi.org/10.1016/0017-9310(90)90148-N

[56] Y. Cao, and A. Faghri, "A numerical analysis of phase-change problems including natural convection," *Journal of Heat Transfer (Transactions of the ASME (American Society of Mechanical Engineers), Series C); (United States)*, Vol. 112:3, 1990.

[57] E.M. Sparrow, S. V. Patankar, and S. Ramadhyani, "Analysis of melting in the presence of natural convection in the melt region," *Journal of Heat Transfer*, Vol. 99, No. 4, pp. 520, 1977. http://dx.doi.org/10.1115/1.3450736

[58] K.A.R. Ismail, and C.A. Melo, "Convection-based model for a PCM vertical storage unit," *International Journal of Energy Research*, Vol. 22, No. 14, pp. 1249–1265, 1998. http://dx.doi.org/10.1002/(SICI)1099-114X(199811)22:14<1249::AID-ER451>3.0.CO;2-M

[59] B.J. Jones, D. Sun, S. Krishnan, and S. V. Garimella, "Experimental and numerical study of melting in a cylinder," *International Journal of Heat and Mass Transfer*, Vol. 49, No. 15–16, pp. 2724–2738, 2006. http://dx.doi.org/10.1016/j.ijheatmasstransfer.2006.01.006

[60] C.W. Robak, T.L. Bergman, and A. Faghri, "Enhancement of latent heat energy storage using embedded heat pipes," *International Journal of Heat and Mass Transfer*, Vol. 54, No. 15–16, pp. 3476–3484, 2011. http://dx.doi.org/10.1016/j.ijheatmasstransfer.2011.03.038

[61] N. Sharifi, C.W. Robak, T.L. Bergman, and A. Faghri, "Three-dimensional PCM melting in a vertical cylindrical enclosure including the effects of tilting," *International Journal of Heat and Mass Transfer*, Vol. 65, No. null, pp. 798–806, 2013. http://dx.doi.org/10.1016/j.ijheatmasstransfer.2013.06.070

[62] H. Shabgard, T.L. Bergman, N. Sharifi, and A. Faghri, "High temperature latent heat thermal energy storage using heat pipes," *International Journal of Heat and Mass Transfer*, Vol. 53, No. 15–16, pp. 2979–2988, 2010. http://dx.doi.org/10.1016/j.ijheatmasstransfer.2010.03.035

[63] M.M. Kenisarin, "High-temperature phase change materials for thermal energy storage," *Renewable and Sustainable Energy Reviews*, Vol. 14, No. 3, pp. 955–970, 2010. http://dx.doi.org/10.1016/j.rser.2009.11.011

[64] Enertron Inc., "http://www.enertron-inc.com/store.asp," pp. Accessed: February 2013, 2013.

[65] C.W. Robak, T.L. Bergman, and A. Faghri, "Economic evaluation of latent heat thermal energy storage using embedded thermosyphons for concentrating solar power applications," *Solar Energy*, Vol. 85, No. 10, pp. 2461–2473, 2011. http://dx.doi.org/10.1016/j.solener.2011.07.006

[66] MEPS International Ltd., "www.meps.co.uk," pp. Accessed: December 2012, 2012.

[67] B. Kelly, and D. Kearney, "Thermal storage commercial plant design study for a 2-tank indirect molten salt system," No. July, pp. 1–32, 2006.

[68] U. Herrmann, B. Kelly, and H. Price, "Two-tank molten salt storage for parabolic trough solar power plants," *Energy*, Vol. 29, No. 5–6, pp. 883–893, 2004. http://dx.doi.org/10.1016/S0360-5442(03)00193-2

[69] G.C. Glatzmaier, *Developing a cost model and methodology to estimate capital costs for thermal energy storage*, National Renewable Energy Laboratory,, 2011.

[70] P. Lamberg, R. Lehtiniemi, and A.-M. Henell, "Numerical and experimental investigation of melting and freezing processes in phase change material storage," *International Journal of Thermal Sciences*, Vol. 43, No. 3, pp. 277–287, 2004. http://dx.doi.org/10.1016/j.ijthermalsci.2003.07.001

[71] National Renewable Energy Laboratory, "System Advisor Model Version 2012.5.11 (SAM 2012.5.11), User Documentation," 2012.

[72] S.H. Goods, and R.W. Bradshaw, "Corrosion of stainless steels and carbon steel by molten mixtures of commercial nitrate salts," *Journal of Materials Engineering and Performance*, Vol. 13, No. 1, pp. 78–87, 2004. http://dx.doi.org/10.1361/10599490417542

[73] H. Shabgard, C.W. Robak, T.L. Bergman, and A. Faghri, "Heat transfer and exergy analysis of cascaded latent heat storage with gravity-assisted heat pipes for concentrating solar power applications," *Solar Energy*, Vol. 86, No. 3, pp. 816–830, 2012. http://dx.doi.org/10.1016/j.solener.2011.12.008

[74] M. De Lucia, and A. Bejan, "Thermodynamics of phase-change energy storage: the effects of liquid superheating during melting, and irreversibility during solidification," *Journal of Solar Energy Engineering*, Vol. 113, No. 1, pp. 2, 1991. http://dx.doi.org/10.1115/1.2929947

[75] H. Shabgard, T.L. Bergman, and A. Faghri, "Exergy analysis of latent heat thermal energy storage for solar power generation accounting for constraints imposed by long-term operation and the solar day," *Energy*, pp. in press, 2013.

[76] T.L. Bergman, A.S. Lavine, F.P. Incropera, and D.P. DeWitt, *Fundamentals of Heat and Mass Transfer*, 7th Edition, Wiley, Hoboken, 2011.

[77] P. Salamon, A. Nitzan, B. Andresen, and R. Berry, "Minimum entropy production and the optimization of heat engines," *Physical Review A*, Vol. 21, No. 6, pp. 2115–2129, 1980. http://dx.doi.org/10.1103/PhysRevA.21.2115

[78] S. Wang, A. Faghri, and T.L. Bergman, "A comprehensive numerical model for melting with natural convection," *International Journal of Heat and Mass Transfer*, Vol. 53, No. 9–10, pp. 1986–2000, 2010. http://dx.doi.org/10.1016/j.ijheatmasstransfer.2009.12.057

[79] P. Jany, and A. Bejan, "Scaling theory of melting with natural convection in an enclosure," *International Journal of Heat and Mass Transfer*, Vol. 31, No. 6, pp. 1221–1235, 1988. http://dx.doi.org/10.1016/0017-9310(88)90065-8

[80] N. Sharifi, S. Wang, T.L. Bergman, and A. Faghri, "Heat pipe-assisted melting of a phase change material," *International Journal of Heat and Mass Transfer*, Vol. 55, No. 13–14, pp. 3458–3469, 2012. http://dx.doi.org/10.1016/j.ijheatmasstransfer.2012.03.023

[81] S. Wang, A. Faghri, and T.L. Bergman, "Numerical modeling of alternate melting and solidification," *Numerical Heat Transfer, Part B: Fundamentals*, Vol. 58, No. 6, pp. 393–418, 2010. http://dx.doi.org/10.1080/10407790.2010.529024

[82] S. Patankar, *Numerical Heat Transfer and Fluid Flow (Hemisphere Series on Computational Methods in Mechanics and Thermal Science)*, McGraw-Hill, New York, 1980.

[83] W.W. Jin, W.Q. Tao, Y.L. He, and Z.Y. Li, "Analysis of Inconsistency of SIMPLE-like Algorithms and an Entirely Consistent Update Technique—The CUT Algorithm," *Numerical Heat Transfer, Part B: Fundamentals*, Vol. 53, No. 4, pp. 289–312, 2008. http://dx.doi.org/10.1080/10407790701703674

[84] J.H. Ferziger, and M. Peric, *Computational Methods for Fluid Dynamics*, 3rd Edition, Springer, New York, 2001.

[85] H.L. Stone, "Iterative solution of implicit approximations of multidimensional partial differential equations," *SIAM Journal on Numerical Analysis*, Vol. 5, No. 3, pp. 530–558, 1968. http://dx.doi.org/10.1137/0705044

[86] S. Wang, A. Faghri, and T.L. Bergman, "Melting in cylindrical enclosures: numerical modeling and heat transfer correlations," *Numerical Heat Transfer, Part A: Applications*, Vol. 61, No. 11, pp. 837–859, 2012. http://dx.doi.org/10.1080/10407782.2012.672895

[87] N. Hannoun, V. Alexiades, and T.Z. Mai, "A reference solution for phase change with convection," *International Journal for Numerical Methods in Fluids*, Vol. 48, No. 11, pp. 1283–1308, 2005. http://dx.doi.org/10.1002/fld.979

[88] P. Le Quéré, and D. Gobin, "A note on possible flow instabilities in melting from the side," *International Journal of Thermal Sciences*, Vol. 38, No. 7, pp. 595–600, 1999. http://dx.doi.org/10.1016/S0035-3159(99)80039-7

[89] J. Mencinger, "Numerical simulation of melting in two-dimensional cavity using adaptive grid," *Journal of Computational Physics*, Vol. 198, No. 1, pp. 243–264, 2004. http://dx.doi.org/10.1016/j.jcp.2004.01.006

[90] V.R. Voller, P. Felix, and C.R. Swaminathan, "Cyclic phase change with fluid flow," *International Journal of Numerical Methods for Heat & Fluid Flow*, Vol. 6, No. 4, pp. 57–64, 1996. http://dx.doi.org/10.1108/09615539610123450

[91] C.J. Ho, and C.H. Chu, "Periodic melting within a square enclosure with an oscillatory surface temperature," *International Journal of Heat and Mass Transfer*, Vol. 36, No. 3, pp. 725–733, 1993. http://dx.doi.org/10.1016/0017-9310(93)80048-Y

[92] C.J. Ho, and C.H. Chu, "A simulation for multiple moving boundaries during melting inside an enclosure imposed with cyclic wall temperature," *International Journal of Heat and Mass Transfer*, Vol. 37, No. 16, pp. 2505–2516, 1994. http://dx.doi.org/10.1016/0017-9310(94)90288-7

List of peer-reviewed journal articles produced during the course of the project:

[1] S. Wang, A. Faghri, T.L. Bergman, A comprehensive numerical model for melting with natural convection, International Journal of Heat and Mass Transfer. 53 (2010) 1986–2000.

[2] H. Shabgard, T.L. Bergman, N. Sharifi, A. Faghri, High temperature latent heat thermal energy storage using heat pipes, International Journal of Heat and Mass Transfer. 53 (2010) 2979–2988.

[3] S. Wang, A. Faghri, T.L. Bergman, Numerical modeling of alternate melting and solidification, Numerical Heat Transfer, Part B: Fundamentals. 58 (2010) 393–418.

[4] C.W. Robak, T.L. Bergman, A. Faghri, Enhancement of latent heat energy storage using embedded heat pipes, International Journal of Heat and Mass Transfer. 54 (2011) 3476–3484.

[5] M. Aghvami, A. Faghri, Analysis of flat heat pipes with various heating and cooling configurations, Applied Thermal Engineering. 31 (2011) 2645-2655.

[6] C.W. Robak, T.L. Bergman, A. Faghri, Economic evaluation of latent heat thermal energy storage using embedded thermosyphons for concentrating solar power applications, Solar Energy. 85 (2011) 2461–2473.

[7] N. Sharifi, T.L. Bergman, A. Faghri, Enhancement of PCM melting in enclosures with horizontally-finned internal surfaces, International Journal of Heat and Mass Transfer. 54 (2011) 4182-4192.

[8] H. Shabgard, A. Faghri, Performance characteristics of cylindrical heat pipes with multiple heat sources, Applied Thermal Engineering. 31 (2011) 3410-3419.

[9] K. Nithyanandam, R. Pitchumani, Analysis and optimization of a latent thermal energy storage system with embedded heat pipes, International Journal of Heat and Mass Transfer. 54 (2011) 4596–4610.

[10] H. Shabgard, C.W. Robak, T.L. Bergman, A. Faghri, Heat transfer and exergy analysis of cascaded latent heat storage with gravity-assisted heat pipes for concentrating solar power applications, Solar Energy. 86 (2012) 816–830.

[11] N. Sharifi, S. Wang, T.L. Bergman, A. Faghri, Heat pipe-assisted melting of a phase change material, International Journal of Heat and Mass Transfer. 55 (2012) 3458–3469.

[12] S. Wang, A. Faghri, T.L. Bergman, Melting in cylindrical enclosures: numerical modeling and heat transfer correlations, Numerical Heat Transfer, Part A: Applications. 61 (2012) 837–859.

[13] S. Wang, A. Faghri, T.L. Bergman, Transient natural convection in vertical annuli: numerical modeling and heat transfer correlation, Numerical Heat Transfer, Part A: Applications. 61 (2012) 823–836.

[14] S. Wang, A. Faghri, T.L. Bergman, A comparison study of sensible and latent thermal energy storage systems for concentrating solar power applications, Numerical Heat Transfer, Part A: Applications. 61 (2012) 860–871.

[15] H. Bahrami, T.L. Bergman, A. Faghri, Forced convective heat transfer in a microtube including rarefaction, viscous dissipation and axial conduction effects, International Journal of Heat and Mass Transfer. 55 (2012) 6665–6675.

[16] K. Nithyanandam, R. Pitchumani, Analysis and design of dye-sensitized solar cell, Solar Energy. 86 (2012) 351–368.

[17] K. Nithyanandam, R. Pitchumani, Computational studies on a latent thermal energy storage system with integral heat pipes for concentrating solar power, Applied Energy. 103 (2013) 400–415.

[18] K. Nithyanandam, Computational modeling of dynamic response of a latent thermal energy storage system with embedded heat pipes, Journal of Solar Energy Engineering. 136 (2013) 011010.

[19] N. Sharifi, C.W. Robak, T.L. Bergman, A. Faghri, Three-dimensional PCM melting in a vertical cylindrical enclosure including the effects of tilting, International Journal of Heat and Mass Transfer. 65 (2013) 798–806.

[20] H. Shabgard, T.L. Bergman, A. Faghri, Exergy analysis of latent heat thermal energy storage for solar power generation accounting for constraints imposed by long-term operation and the solar day, Energy. (2013) in press.